Computers and Geotechnics

3D modelling of soil-rock mixtures considering the morphology and fracture characteristics of breakable blocks

--Manuscript Draft--

Manuscript Number:	COMGE-D-20-01364R1
Article Type:	Research Paper
Keywords:	soil-rock mixture; random block generation; random fracture generation; 3D S-RM DEM model; mechanical behaviour of S-RM
Corresponding Author:	Han Zhang China University of Geosciences(Wuhan) Wuhan, Hubei CHINA
First Author:	Xinli Hu, Dr.
Order of Authors:	Xinli Hu, Dr.
	Han Zhang
	Daniela Boldini, Dr.
	Chang Liu, Dr.
	Chuncan He, Dr.
	Shuangshuang Wu, Dr.
Abstract:	Failure mechanisms of a soil-rock mixture (S-RM) can be efficiently investigated by the discrete element method (DEM). This paper proposes a stochastic approach for 3D DEM modelling of S-RM samples accounting for morphological features and internal fractures characteristics of breakable blocks. The research refers to an artificial S-RM filling slope, mainly containing highly-weathered shale blocks, located in the Yunnan Province, China. The 3D morphological features of the blocks and the characteristics of their internal fractures were obtained by CT technology and image processing. A stochastic method based on harmonic series was developed, allowing the generation of random block clusters with characteristics similar to the original ones. Another stochastic approach was implemented for the creation of the internal fractures, simulated as voids in the block clusters, following the characteristic of the real fractures. Finally, the procedure was applied for the definition of a 3D S-RM DEM model with 40% block proportion, whose meso-parameters were determined for simulating direct shear tests.The numerical results showed that the generated random S-RM DEM model well reproduced the experimental behaviour of S-RM samples with breakable blocks. Also, they highlighted the importance of modelling the block breakage and internal fractures by companion simulations.

Powered by Editorial Manager® and ProduXion Manager® from Aries Systems Corporation

Dear editorial board of Computers and Geotechnics,

Please find enclosed the revised manuscript: “3D modelling of soil-rock mixtures considering the morphology and fracture characteristics of breakable blocks”, by Han Zhang, et al., for a possible publication as a Research Paper in Computers and Geotechnics. All co-authors cooperated and agreed with the contents of the manuscript. We certify that the submission is an original work and is not under review in any other journals.

We have performed the revisions according to the suggestions by the editors and reviewers, the revised portions are marked in red in the manuscript.

Sincerely yours,

Corresponding author: Han Zhang

Faculty of Engineering, China University of Geosciences , Wuhan , 430074, China

Email address: zhanghan@cug.edu.cn.

Response of Reviewers comments

We thank the Reviewers for their valuable comments concerning our manuscript. They were all helpful for improving our paper. We studied all comments carefully and made the requested corrections, which we hope will meet their approval. Revised portions are marked in red in the manuscript. The main corrections and the reply to the Reviewers' comments are as follows:

Reviewer 1

Comment#1: 1. L13-16 of Page 4. The following relevant papers on X-ray CT characterization of 3D contact fabric and grain kinematics of sands under shear might be worthy of a mention:

[i] Cheng, Z., & Wang, J. (2018). Experimental investigation of inter-particle contact evolution of sheared granular materials using X-ray micro-tomography. Soils and Foundations, 58(6), 1492-1510.

[ii] Cheng, Z., & Wang, J. (2018). A particle-tracking method for experimental investigation of kinematics of sand particles under triaxial compression. Powder Technology, 328, 436-451.**Response#1:**

Thanks for your recommendation: these relevant papers were introduced in Section 1.

Comment#2: L18-20 of Page 4. 'However, the exact one-to-one mapping of the CT images into the corresponding model is clearly an unfeasible choice …' It may be worthwhile to refer to the following work on DEM modeling of sand based on one-to-one mapping of CT images:

[iii] Wu M., et al. (2020). DEM modelling of mini-triaxial test based on one-to-one mapping of sand particles. Géotechnique, 1-14.

Response#2:

We referred to this paper in Section 1 as follows:

The exact one-to-one mapping of the CT images were used to establish a DEM model of a mini-triaxial sand specimen 8 mm in diameter and 16 mm in heigth (Wu et al., 2020). However, this approach cannot be followed at the moment for modelling large-scale samples, as the S-RM ones used in the discussed in-situ tests.

Comment#3: I think there is a mistake in Line 6 of Page 6. Referring to Fig. 2a, diameter is 145 mm and height is 285 mm?

Response#3:

Yes, the text was corrected into "The pipes, labelled as C1, C2 and C3 (Fig. 2a), had a diameter of 145mm and a height of 285mm.".

Comment#4: Line 13-14 of Page 6. Does the 3D CT image have a voxel size of 0.45 mm×0.45 mm×0.6 mm? I think it is better to use' voxel size' instead of 'pixel size' here.

Response#4:

Yes, the voxel size of a 3D CT image is 0.45 mm×0.45 mm×0.6 mm. We agree with the reviewer that the use of "voxel size" is more accurate than "pixel size" and we revised the manuscript accordingly.

Comment#5: Fig. 3a- Referring to your median filter size, I guess your image processing is implemented on 3D images. Am I right? It should be clarified in the text.

Response#5:

Yes, the image processing was performed on the 3D CT images, referring not only to the median filter but also to the 26-neighborhood connected components extraction and watershed-based separation. This point was clarified it in the revised manuscript.

Comment#6: Figs. 10b & 10c suggest that S_p and R are scale-dependent, i.e., the accuracy of S_p and R are dependent on the grain size. The reason should be explained in the text.

Response#6:

Figure 10c & 10d reveals that S_p and R are more difficult to be described, necessitating a higher value of n, especially for the blocks with the larger particle size. This is because these larger blocks are characterised by a larger angularity and more complex morphological details (see Figure 4c), indicating the description of the block surface with larger size needs more harmonics series than the smaller one. This explanation was added to the text following the reviewer's suggestion.

Comment#7: Fig. 7b What does N_f in the y axis represent? Should it be F_f? Does F_f of Eqs. 7, 10 and 11 refer to the same thing, i.e., fracture number? It should be mentioned in Eq.7 that the calculation based on this equation could lead to non-integer values.

Response#7:

We thank the reviewer for having found this mistake that we promptly corrected. In fact, in the Fig. 7b, the label of y axis is F_f instead of N_f. The F_f in the Eqs. (7), (10) and (11) all refer to fracture frequency. It was mentioned in the text: the F_f calculated by Eqs. (7), (10) and (11) maybe non-integer values**.**

Comment#8: The number of '5.2' of Fig. 5a is not consistent with '5.3' in Eq. 7.

Response#8:

Again, we thank the reviewer for his careful correction. Yes, the mean value of the Gaussian function in Eq. 7 is 5.2, as shown in Fig. 5a.

Comment#9: Line 24 of Page 18. The version of the particle flow code software should also be specified.

Response#9:

The version of the particle flow code used in the simulation of the soil-rock mixtures is PFC^{3D}5.0, now specified in the revised manuscript.

Comment#10: Line 9 of Page 19. 'The maximum fracture size is 0.8 mm'? Please verify whether this is correct.

Response#10:

We corrected the text into “The minimum fracture size is 0.8 mm”.

Comment#11: Page 24 of Section 4. The soils with a grain size range of 4.8-5.0 mm were generated in the DEM model. It seems that the realistic morphologies were not considered in the DEM modeling for soil grains, while those were modelled for the blocks. Why? The reasons should be mentioned in the paper.

Response#11:

In our study, the soil particles were simplified as sphere balls in the S-RM DEM models, similarly to other DEM studies of S-RM (e.g. Xu et al., 2016b). This simplification is mainly due to the limited computation capacity. Although the morphology of soil particles can be represented by bonding several smaller balls, this will lead to a large increase in the particle number in the DEM model. As such, the irregular morphology of soil particles was neglected and the rolling resistant model was adopted for simulating their roughness (Jiang et al. 2005, Xu et al. 2016b).

Comment#12: The paper needs to be carefully proofread to eliminate all typos and grammar errors. See for example:

Line 22 of Page 5: 'wan' should be 'was'?

Line 11 of Page 15: 'serious' should be 'series'

Line 2 of Page 18: 'fuction' should be 'function'.

Line 11 of Page 18: 'Similarly' should be 'Similar'

Response#12:

We thank the reviewer for these careful checks. Spelling mistakes were corrected and the text was checked again.

Reviewer 2

Comment2#1: Eqs. (3) and (6) are purely empirical and dimensional consistency is not satisfied. Therefore, the unit of D in this equation should be clarified.

Response2#1:

The unit of the particle size of blocks D in Eqs. (3) and (6) is in mm. The revised manuscript was corrected accordingly.

Comment2#2: Explanation to the observed relative orientation distributions of fractures, as shown in Fig. 7, should be given.

Response2#2:

The θ values mainly lie in the ranges 0 ° - 40 ° and 120 ° - 180 °, while γ in the 30 ° - 70 ° one. This is because the inter-fractures commonly formed along the stratification orientation of the shale blocks under the compaction stage during the slope filling.

Comment2#3: In the DEM analyses, soil particles are modelled as balls and irregular morphology of the particles is not taken into account. Limitation of the assumption should be addressed.

Response2#3:

The limitation was mentioned in the text:

Considering of the limitation of the computation capacity, the soil particles in the DEM model were simplified as spherical balls having radii from 4.8 mm to 5.0 mm. Although the morphology of soil particles can be represented by bonding several smaller balls, this will lead to a large increase in the particle number in the DEM model. As such, the irregular morphology of soil particles was neglected and the rolling resistant model was adopted for simulating their roughness (Jiang et al. 2005, Xu et al. 2016b).

Highlights

1. A stochastic generation approach, accounting for the morphological features and internal fractures characteristics of breakable blocks, was proposed and applied to the 3D DEM modelling of S-RM.

2. A stochastic method was developed for generating random blocks with characteristics similar to the real ones on the basis of spherical harmonic series.

3. A stochastic approach was proposed for creating random fractures on the basis of the characteristics of the real ones.

4. It was demonstrated that neglecting block breakage and the presence of internal fractures had significant influence on the shear strength of the S-RM sample by companion simulations.

Manuscript

3D modelling of soil-rock mixtures considering the morphology and fracture characteristics of breakable blocks

Xinli Hu[1], Han Zhang[1]*, Daniela Boldini[2], Chang Liu[1], Chuncan He[1], Shuangshuang Wu[1]

1. Faculty of Engineering, China University of Geosciences, Wuhan, 430074, China

2. Department of Chemical Engineering Materials Environment, Sapienza University of Rome, Via Eudossiana 18, 00184 Rome, Italy

* Corresponding author, e-mail: zhanghan@cug.edu.cn

ABSTRACT

Failure mechanisms of a soil-rock mixture (S-RM) can be efficiently investigated by the discrete element method (DEM). This paper proposes a stochastic approach for 3D DEM modelling of S-RM samples accounting for morphological features and internal fractures of blocks and their potential breakage. The research refers to the case-history of an artificial S-RM filling slope, mainly containing highly-weathered shale blocks, constructed at the ±500kV electronic converter station in the Funing County, Yunnan Province, China. The 3D morphological features of the blocks and the characteristics of their internal fractures were obtained by CT technology and image processing. A stochastic method based on harmonic series was developed starting from the real blocks, allowing the generation of random block clusters with characteristics similar to the original ones. Another stochastic approach was implemented for the creation of the internal fractures, simulated as voids in the block clusters, following the characteristic of the real fractures. Finally, the procedure was applied for the definition of a 3D S-RM DEM model with 40% block proportion, whose meso-parameters were determined for simulating direct shear tests. These latters were also useful to explore the mechanical response of the sample at the meso-scale, including the formation and development of the localization band. The numerical results showed that the generated random S-RM DEM model well reproduced the experimental behaviour of S-RM samples with breakable blocks. Also, they highlighted the importance of modelling the block breakage and internal fractures; in fact, companion simulations with unbreakable blocks and breakable blocks without fractures were all characterised by increased shear strength with higher friction angle but reduced cohesion.

Key words: soil-rock mixture; random block generation; random fracture generation; 3D S-RM DEM model; mechanical behaviour of S-RM

1. Introduction

Soil-rock mixtures (S-RMs) were defined by Xu (2008) as extremely inhomogeneous geomaterials composed of rock blocks, with various sizes and a relative high strength, and a fine-grained soil matrix. The rock-matrix interface is unbounded in the S-RMs, in contrast to bimrocks (Medley, 1994). S-RMs are widespread in natural landslides (Sonmez, 2006; Xu et al., 2007; Yang et al., 2019) but are also commonly used as filling materials in embankments and artificial slopes (Calseira & Brito, 2014; Zhang et al., 2016; Cen et al., 2017). To assess the stability of such geo-structures, several researches have investigated their mechanical properties by laboratory (Dong, 2007; Hamidi et al., 2011; Liu et al., 2017) and in-situ (Xu et al., 2011; Coli et al., 2011; Zhang et al., 2016; Zhang et al., 2020) tests. The experimental evidence has shown that the mechanical properties of S-RMs are not only controlled by the volumetric block proportion (*VBP*), but also by block shape and strength, this latter affected by the potential presence of pre-existing internal fractures. However, the analysisof all the complex failure mechanisms occurring during the experiments, including those controlled by the shape and strength of the rock blocks, is practically unfeasible.

Numerical modelling, and especially the discrete element method (DEM) approach, is undoubtedly a powerful tool for revealing the failure mechanisms in S-RMs. However, accuracy of calculations is strictly connected to the capacity of the numerical model to reasonably account for the peculiar characteristics of these materials, including those related to the shape of the rock blocks and to the possible presence of pre-existing fractures.

Nowadays, 2D numerical S-RM models are mainly generated following two possible strategies, the first one making use of stochastic algorithms (Li et al. 2004; Xu et al., 2016a; Chen et al., 2018) and the other one based on digital image processing (DIP) (Yue et al., 2003; Xu et al., 2008; Hu et al., 2018). Li et al. (2004) created S-RM stochastic numerical models using the Monte Carlo random sampling principle, the spatial distribution and size distribution of rock blocks obeying an even and a normal distribution law, respectively. A multi-circle block generation method, adopted for the subsequent generation of 2D DEM S-RM models, was developed by Xu et al. (2016a) considering the size distribution and spatial location of rock blocks. Chen et al. (2018) proposed an aggregate structure generation method based on an enhanced procedure of random sequential addition, significantly reducing the computational cost, and established S-RM models with a high *VBP*. In all these stochastic S-RM models, the shape of rock blocks is that of simple convex polygons, ignoring their real morphology**.** In order to overcome this limitation, Yue et al.

(2003) used digital image processing (DIP) for generating 2D FEM models in which rock blocks with real shapes were derived from 2D images. The DIP technique was also employed in the set-up of 2D DEM models of S-RMs by Xu et al. (2008) and Hu et al. (2018).

3D numerical models, more representative of the real structure of S-RMs and bimrocks, have been also recently developed. Cheng et al. (2010) created 3D S-RM DEM models with different *VBP* on the basis of the particle bonding method, the blocks deriving from the bonding of a group of elementary spheres. Coli et al. (2012) proposed 3D FEM bimrock models containing different ellipsoidal (e.g. prolate, sphere and oblate) rock blocks for the simulation of uniaxial and triaxial compression tests. Xu et al. (2016b) developed 3D random systems and established 3D DEM S-RM models, with no overlap between two bonded spheres in a convex polyhedron rock block clump, for the analysis of failure mechanisms of S-RMs during direct shear tests. Nevertheless, the shape of rock blocks in these 3D numerical models is also limited to that of simple polyhedrons.

The X-ray computed tomography (CT) technology has been widely used for the 3D visualization and characterisation of the shape and structure of geomaterials (e.g. Masad et al., 2005; Fonseca et al., 2012; Zhao et al., 2015), generating 3D numerical models of sand assembly (Zhou et al., 2016; Zhou & Wang, 2017; Xu et al., 2020), and investigating the movement and contact evoluation characteristics of sand particles in the shear process under the triaxial compression (Cheng & Wang, 2018a; b). Some features of rock fractures, such dimension, roughness and spatial distribution were investigated using CT images by Kolyukhin et al. (2014) and Liang et al. (2016). The exact one-to-one mapping of the CT images were used to establish a DEM model of a mini-triaxial sand specimen 8 mm in diameter and 16 mm in heigth (Wu et al., 2020). However, this approach cannot be followed at the moment for modelling large-scale samples, as the S-RM ones used in the discussed in-situ tests. Relatively few researches have established reasonable stochastic approaches for the definition of rock block models considering real 3D multi-scale morophological features, such as the roundness in addition to dimension and sphericity. Furthermore, the internal structure of rock blocks, related to the presence of fractures and voids, has still never been accounted for.

This study proposes an experimental-mathematical approach for the generation of 3D DEM S-RM models accounting for block morphology and characteristics of block internal fractures. The research refers to the case-history of an artificial S-RM filling slope constructed at the ±500kV electronic converter station in the Funing County, Yunnan Province, China. The filling material adopted at the site mainly consisted in a sandy silt matrix and highly-weathered shale blocks. For an economic and safe design, some large-scale direct shear tests were performed for assessing the shear strength properties of the S-RMs. After testing, a limited number (e.g. 300) of shale blocks of different sizes (10 - 80 mm) were scanned and reconstructed, on the basis of CT technology and image processing, for obtaining their morphological features and the characteristics of their internal fractures. Stochastic methods were developed, using SH series and characteristic distributions of real blocks and fractures, for establishing random blocks and fractures with characteristics similar with the real ones. DEM models were then implemented simulating the blocks as clusters and the fractures as voids. In particular, a S-RM DEM model with 40% *VBP* was considered to analyse the mechanical response of the material during direct shear tests.

2. Morphological characteristics of the shale blocks and of their internal fractures

2.1 3D CT reconstruction of shale blocks

2.1.1 Shale blocks in the S-RM samples

The considered S-RM is mainly composed of sandy silt matrix and highly-weathered shale blocks, as shown in Fig. 1a. The shale blocks are made of 76.15% of quartz and 23.85% of chlorite, with average values of dry density ρ_d = 1.577 g/cm^3, particle weight G_S = 2.902, porosity n = 36.5 % and unconfined compressive strength UCS = 4.3±1.5 MPa (Zhang et al., 2020).

During the construction of the electronic converter station, one of the artificial slopes experienced large lateral displacements due to the overestimation of the shear strength of the S-RM at the design stage. As such, some large-scale direct shear tests (DST) were performed with a cylindrical shear box 400 mm in height and 560 mm in diameter (Fig. 1b). The threshold particle diameter d_{thr}, formally separating the matrix from the blocks, was defined following Medly (1994) as d_{thr} = 0.05 L_c, where L_c is the characteristic engineering scale. Specifically, L_c was taken equal to the apparatus half height, equal to 200 mm, providing a threshold value of 10 mm. The maximum particle size of the blocks, collected from the artificial slope, was not larger than 80 mm, corresponding to 1/5 of the semi-height of shear box. The tested S-RM samples were characterised by a *VBP* of 35% - 60%.

(a) Shale blocks in the S-RM **(b) large-scale direct shear apparatus**

Fig. 1 Shale blocks employed in the artificial slope and the large-scale direct shear apparatus

2.1.2 3D CT reconstruction

CT technique was applied to reconstruct the 3D morphology of the blocks and the main features of the fractures. About 250 undisturbed (i.e. not affected by the failure process) shale blocks ranging from 10 mm to 80 mm were randomly picked from the S-RM samples after the DSTs and placed into three PVC pipes for CT scanning. The pipes, labelled as C1, C2 and C3 (Fig. 2a), had a diameter of 145mm and a height of 285mm. Foam particles of very low density were adopted to fill the pipes and isolate the blocks. The Siemens Somatom Sensation 40 CT system (Fig. 2b), provided by the Key Laboratory of Geotechnical Mechanics and Engineering of the Ministry of Water Resources, Yangtze River Scientific Research Institute, was employed to perform the X-ray CT scanning and acquire a series CT images. As shown in the CT image of Fig. 2c, the blocks and their internal fractures were clearly observed. Each of these images consisted of 512 voxels by 512 voxels, with a resolution of 0.45 mm/voxel and a thickness of 0.6 mm. The voxel size of the 3D CT image is 0.45 mm×0.45 mm×0.6 mm.

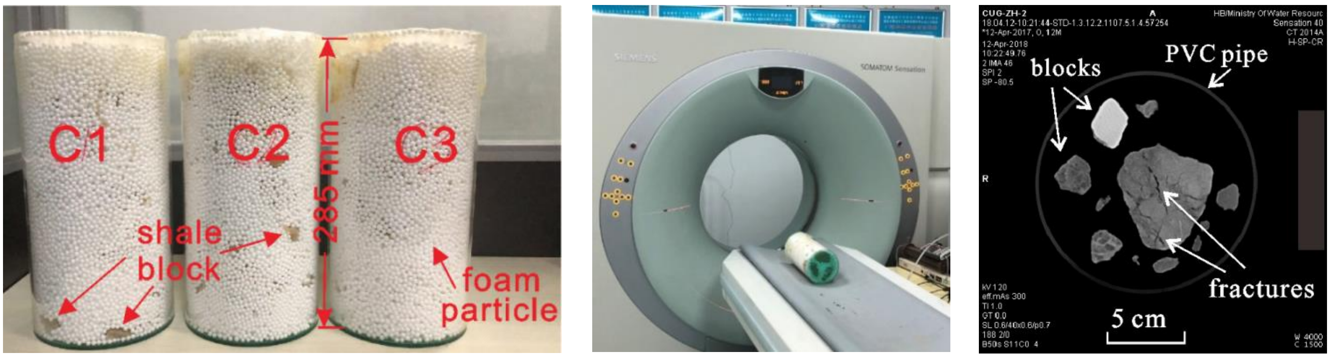

(a) CT samples of shale blocks **(b) CT system** **(c) CT tomographic image**

Fig. 2 Image acquisition using X-ray CT technology

The individual blocks and the fractures were extracted from the CT images by following a series of processing steps, consisting in segmenting the different portions, reducing the noise, separating and labelling individual objects, as summarised in Fig. 3a. The image processing was implemented on 3D images, referring not only to the median filter but also to the 26-neighborhood connected components extraction and watershed-based separation. The triangle meshed surfaces of one block is shown in the Fig. 3b.

The CT images of the fractures were obtained by inverting the binary CT images and removing the connected component representing the background, characterised by the highest number of voxels. Then, the surfaces of internal fractures in a block were reconstructed (Fig. 3c) by performing the same image process.

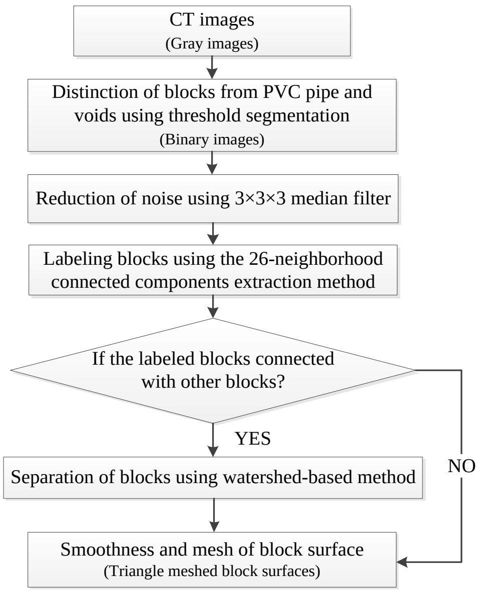

(a) Flowchart of image processing of CT reconstruction

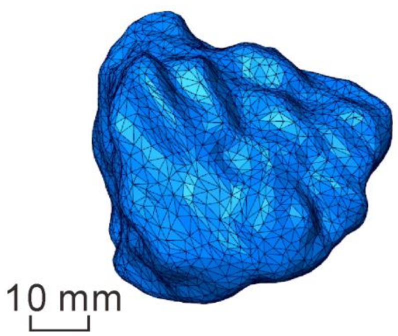

(b) 3D morphological reconstruction of block

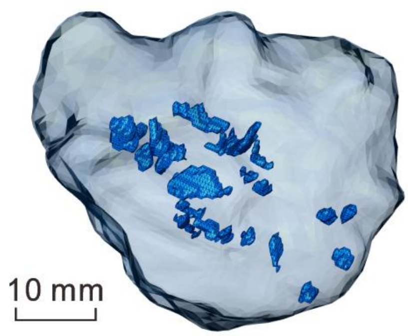

(c) 3D morphological reconstruction of fractures

Fig.3 Image processing and 3D CT reconstruction of block and fracture surfaces

2.2 3D morphological features of the shale blocks

The morphological features of particles can be described, from the largest to the smallest scale, in terms of form, roundness and surface texture (Barrett, 1980; ISO, 2008). The particle form is typically assessed in terms of principal dimensions (and related elongation and flatness) and sphericity (Zheng & Hryciw, 2015). They are defined as described in the following.

(1) Elongation and Flatness

The 3D principal dimensions, named long l_a, intermediate l_b and short l_c axis dimension, can be obtained by the so-called principal component analysis of the particle vertices (Fu et al., 2018). In this paper, the principle intermediate dimension l_b was considered as the block particle size D . The block principal dimensions were used to assess the block form by two widely used descriptors: the elongation index (*EI*) and the flatness index (*FI*), with $EI= l_b/ l_a$ and $FI= l_c/ l_b$. The block form was commonly defined according to the four categories: spheroid (if $EI > 2/3$ and $FI > 2/3$), oblate (if $EI > 2/3$ and $FI < 2/3$), prolate (if $EI < 2/3$ and $FI > 2/3$), and blade (if $EI < 2/3$ and $FI < 2/3$). As shown in Fig. 4a, the shale blocks considered in this study are mainly spheroidal and oblate, with only few prolate and blade. Their *EI* index is in the range 0.5 to 1.0, while the corresponding *FI* values vary from 0.4 to 1.0. The principle dimensions of the blocks were found to obey the following rules:

$$\begin{cases} D \le l_a \le 2D \\ 0.4D \le l_c \le D \end{cases} \tag{1}$$

(2) Sphericity

Sphericity (S_p) can be used for evaluating how much a block resembles a sphere. It is defined as the ratio of the surface area of a sphere, having same volume V of the block particle, to the actual block surface area S:

$$S_p = \frac{\sqrt[3]{36\pi V^2}}{S} \tag{2}$$

The sphericity S_p of blocks are in the range of 0.7 - 0.97, with smaller values for larger D (Fig. 4b), indicating that smaller blocks are more similar to a sphere than the larger ones. The two quantities S_p and D are always bounded by two lines having the following equations:

$$-0.0006D + 0.730 \le S_p \le -0.0014D + 0.984 \tag{3}$$

where the unit of D is mm.

(3) Roundness

Roundness is a descriptor representing the particle angularity (Wadell, 1932), being blocks with smaller roundness those having higher angularity. The 3D roundness was calculated in previous researches (Bullard & Garboczi, 2013; Zhou et al., 2017) by the maximum curvatures κ_{max} of particle surface vertices. The κ_{max} of a vertex of the block surface can be calculated on the basis of Gaussian curvature and mean curvature; the corresponding minimum curvature radius $r_{min}=|\kappa_{max}|^{-1}$ can be used to estimate whether a vertex on the block surface is a 'corner':

$$g(\kappa)=\begin{Bmatrix} 1 & \text{if} & r_{min}<r_{ins} \\ 0 & \text{if} & r_{max}\geq r_{ins} \end{Bmatrix} \tag{4}$$

The function g, called corner judgment function, is equal to 1 or 0 if the vertex is a 'corner' or not, respectively, and r_{ins} is the radius of the maximum inscribed sphere of the block particle. The 3D roundness R of the block particle is then obtained as:

$$R=\frac{\sum_{i=1}^{n} g_i(\kappa)\, r_{min}^{i}}{N r_{ins}} \tag{5}$$

where $g_i(\kappa)$ and r_{min}^{i} represent the corner judgment and the minimum curvature radius of the ith vertex on the block surface, respectively. n and N are the number of vertices and corners on the block surface, respectively.

As shown in Fig. 4c, shale blocks with larger particle size have also larger angularity. The 3D roundness R of blocks varies from 0.3 to 0.8, and the values of R and D lie in the range:

$$-0.00315D+0.489\leq R\leq -0.0039D+0.885 \tag{6}$$

where the unit of D is mm.

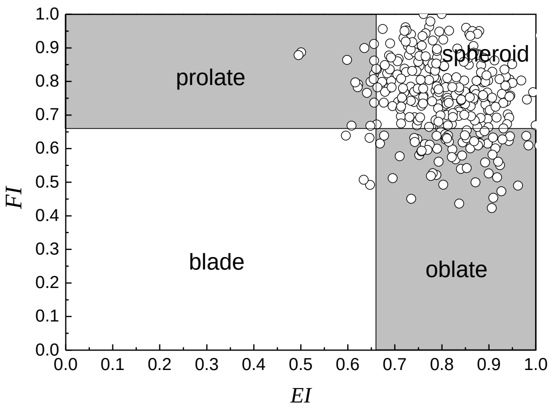

(a) *EI* and *FI* features

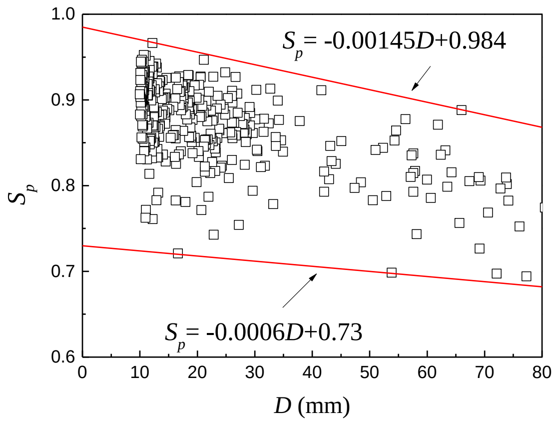

(a) Sphericity features

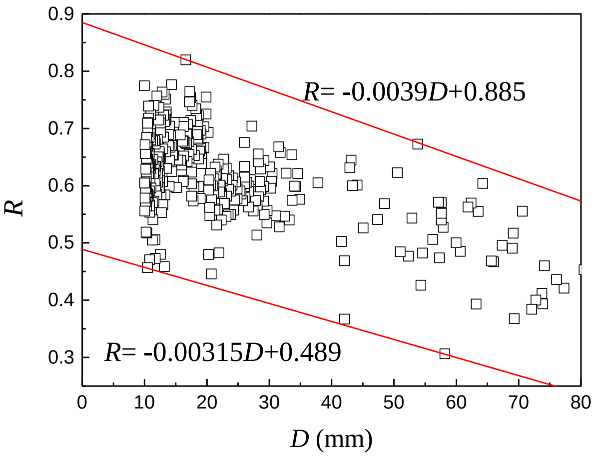

(c) Roundness features

Fig. 4 3D morphlogical features of real shale blocks

2.3 Characteristics of the fractures in the real blocks

(1) Fracture frequency

The fracture frequency F corresponds to the number of fractures in each block, N_f, per unit block volume V. N_f was obtained by the CT reconstructed real fractures: no fractures were found in the blocks with size D less than 40 mm, while N_f varies from 0 to 31 in the larger blocks with a D value ranging from 40 to 80 mm. In general, the average fracture frequency is 0.1 for 1 cm^3.

(2) Size distribution of fractures

The 3D principal dimensions of fractures, indicated respectively with the symbols l_{fa} l_{fb} and l_{fc} for the long, intermediate and short dimensions were obtained by employing the principal component analysis of the fracture vertices.

l_{fa} values distribute from 2 mm to 16 mm, well obeying to an Amplitude Gaussian distribution with $l_{fa} \sim y_0+A \bullet N(\mu, \sigma^2)$, where y_0 and A are the offset and amplitude, and $N(\mu, \sigma^2)$ is a Gaussian function with mean μ and standard deviation σ. The distribution of fracture frequency F_f with l_{fa} values can be expressed by:

$$F_f = 6.1+228.1N(5.2,1.5^2) = 6.1+228.1 \bullet \frac{1}{\sqrt{2\pi} \bullet 1.5} e^{-\frac{(l_a-5.2)}{2 \bullet 1.5^2}}, \quad 2\text{ mm} \le l_a \le 16\text{ mm} \tag{7}$$

Values of l_{fb} and l_{fc} are respectively in the range of 1.5 - 12 mm and 0.8 - 8 mm. It is evident that the larger the dimension l_{fa}, the larger the dimensions l_{fb} and l_{fc} (Fig. 5b and 5c). In fact, l_{fb} and l_{fc} are bounded by the following expressions:

$$0.74l_{fa} - 4.88 \le l_{fb} \le 0.66l_{fa} + 2.98 \tag{8}$$

$$0.56l_{fa} + 0.74 \le l_{fc} \le 0.19l_{fa} \text{-}0.44 \quad (9)$$

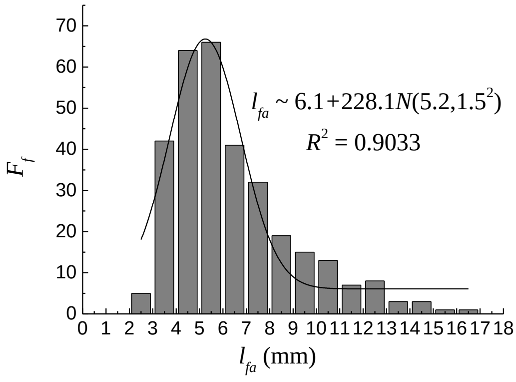

(a) Distribution of l_{fa}

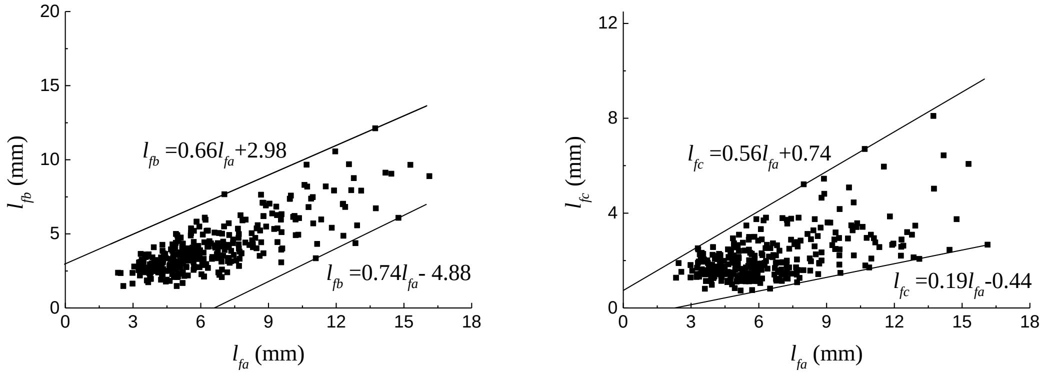

(b) Relationship between l_{fb} and l_{fa} **(c) Relationship between l_{fc} and l_{fa}**

Fig. 5 3D Size distributions of fractures

(3) Distribution of fracture relative orientations

The relative orientation of a fracture in the block is defined in Fig. 6, where the x, y and z axes are the short, intermediate and long axes of a block, respectively, and the z_c axis is the long axis of the internal fracture. θ is the relative angle between the long axis of block and that of fracture, while γ is the angle between the projection of z_c on the xy plane and intermediate axis of block. They are both defined in the interval [0°, 180°].

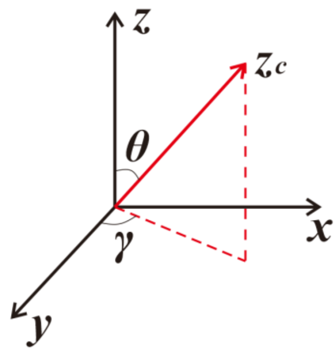

Fig. 6 Schematic of fracture relative orientations in blocks

The relative orientations of fractures and their distribution features are shown in Fig. 7a and 7b. The θ values mainly lie in the ranges 0 ° - 40 ° and 120 ° - 180 °, while γ in the 30 ° - 70 ° one. This is because the inter-fractures commonly formed along the stratification orientation of the shale blocks under the compaction stage during the slope filling. Inspection of Figure 7c reveals that no relationship exists between θ and γ. The distributions of fracture orientations are also found to obey Amplitude Gaussian distributions with Eq. (10) and Eq. (11). The fracture frequency F_f calculated by the Eqs. (7), (10) or (11) maybe non-integer values.

$$F_f = 26.8\text{-}1441.5 \bullet \frac{1}{\sqrt{2\pi \bullet 22.7}} \mathrm{e}^{-\frac{(\theta-70.2)^2}{2 \bullet 22.7^2}} \quad , \quad 0° \le \theta \le 180° \tag{10}$$

$$F_f = 15.6+575.3 \bullet \frac{1}{\sqrt{2\pi \bullet 15.3}} \mathrm{e}^{-\frac{(\gamma-53.0)^2}{2 \bullet 15.3^2}} \quad , \quad 0° \le \gamma \le 180° \tag{11}$$

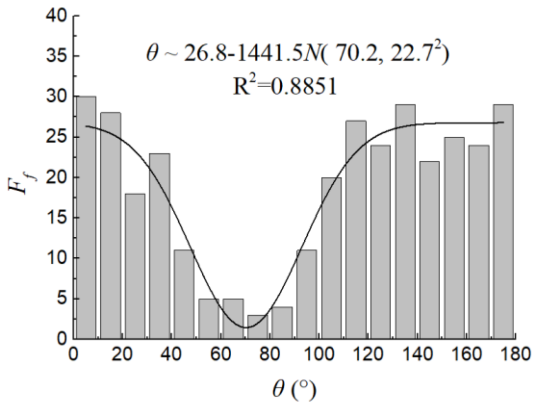

(a) Distribution of θ

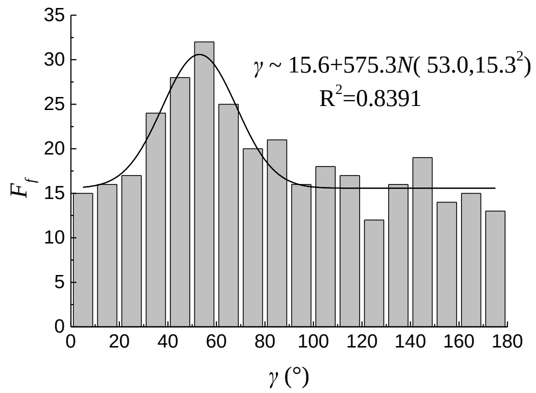

(b) Distribution of γ

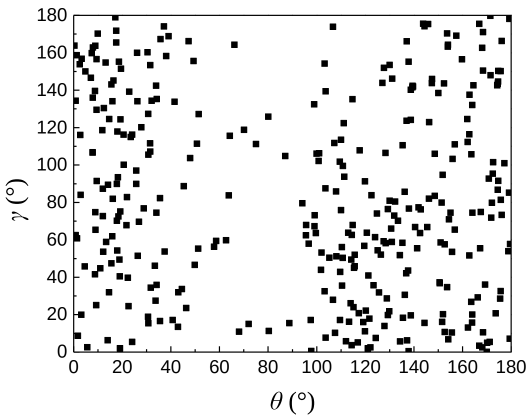

(c) Relationship between fractures relative orientations

Fig. 7 Relative orientation distributions of fractures

3. Generation approaches of 3D random block and fracture models

Due to the large number of rock blocks in the S-RM samples tested in the laboratory, their single scanning was practically unfeasibile. In order to overcome this limitation, block and fracture stochastic generation approaches were proposed, respectively based on spherical harmonics (SH) series of the real blocks and characteristics of the real fractures, and applied to the generation of S-RM DEM models (Fig. 8).

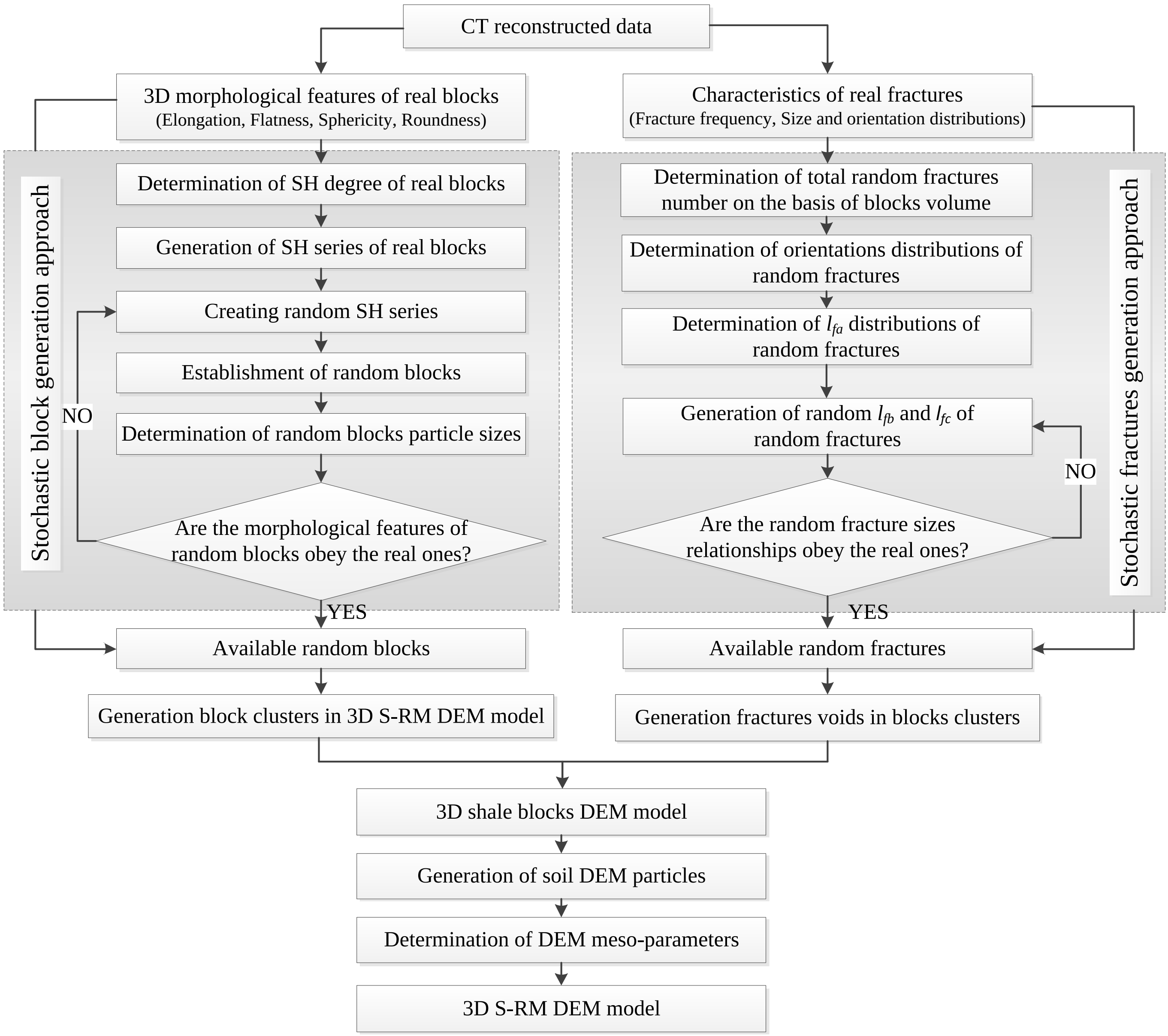

Fig. 8 Flowchart of generation approach of 3D DEM modelling of S-RM samples

3.1 Stochastic block generation approach

3.1.1 Spherical harmonic series of blocks

The spherical harmonic (SH) series were used in the past to represent and quantify the shape of aggregates, rock blocks and sand particles on the basis of 3D CT data (Garboczi, 2002; Masad et al., 2005; Zhou et al., 2015, 2017; Su & Yan, 2018;Feng et al.,2020). Correspondingly, a new block particle can be constructed if a set of spherical harmonic series are created.

The goal of a SH analysis is to expand the polar radius from a unit sphere to the particle surface. The SH series can be expressed as:

$$r(\theta,\phi)=\sum_{n=0}^{\infty}\sum_{m=-n}^{n}a_n^m Y_n^m(\theta,\phi) \tag{12}$$

where $r(\theta, \phi)$ is the polar radius from the particle centre to its surface vertices ($0 \le \theta \le \pi$, $0 \le \phi \le 2\pi$) and a_n^m are the associated SH coefficients. $Y_n^m(\theta,\phi)$ is the SH function given by:

$$Y_n^m(\theta,\varphi)=\sqrt{\frac{(2n+1)(n-m)!}{4\pi(n+m)!}}P_n^m(\cos\theta)e^{im\varphi} \tag{13}$$

$P_n^m(x)$ is the associated Legendre function expressed as:

$$P_n^m(x)=\frac{(-1)^m}{2^n n!}(1-x^2)^{m/2}\frac{\mathrm{d}^{n+m}}{\mathrm{d}x^{n+m}}(x^2-1)^n \tag{14}$$

where n and m are the SH degree and order of $P_n^m(x)$. Note that n is a non-negative integer from zero to infinity according to the required fitting precision, while m is the integer from $-n$ to n so that the total number of a series of a_n^m is $(n+1)^2$.

3.1.2 Determination of SH degree of blocks

As shown in Fig. 9, the morphological features of blocks constructed by the SH series depend on the SH degree n, having the block with higher n an increasing level of resemblance to the CT one. In order to ensure that the morphological features of the SH reconstructed blocks are sufficiently similar with those of real ones, the value of n was fixed reasonably, as discussed in the following.

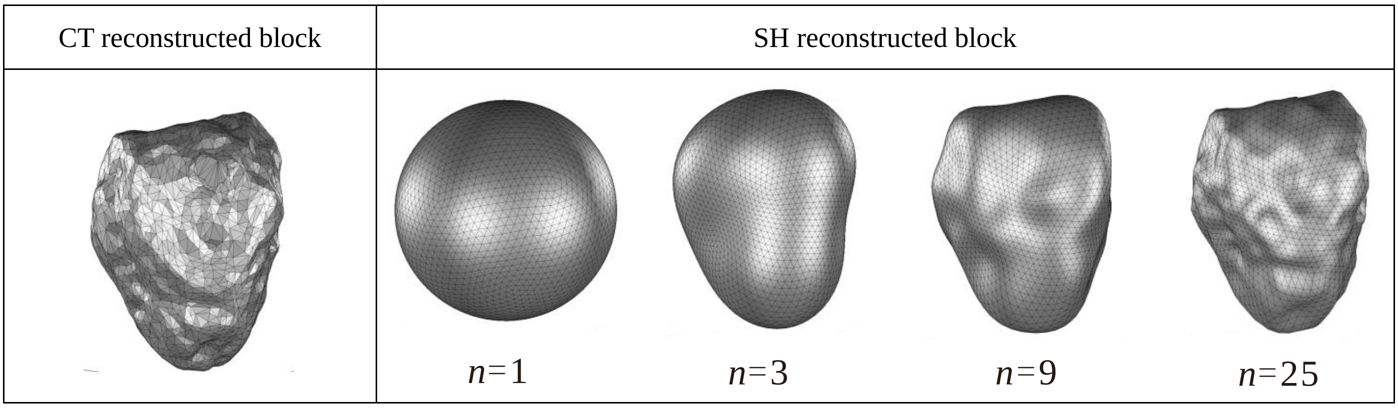

Fig. 9 View of CT reconstructed block and SH reconstructed ones with different SH degrees

Four CT reconstructed blocks, labelled as R1, R2, R3 and R4, with particle size of 75 mm, 41 mm, 28 mm and 14 mm respectively, were selected for assessing the optimum value of *n*. The relative error E_{EI} in the *EI* values of the SH reconstructed blocks to that of the CT ones is defined as:

$$E_{EI} = \frac{\left| EI_{SH} - EI_{CT} \right|}{EI_{CT}} \times 100\% \tag{15}$$

where EI_{SH} and EI_{CT} are the *EI* of the SH reconstructed block and that of the CT one, respectively. Similarly, relative errors for *FI*, S_p and *R* of the SH reconstructed blocks, named respectively as E_{FI}, E_{Sp} and E_R, can also be defined.

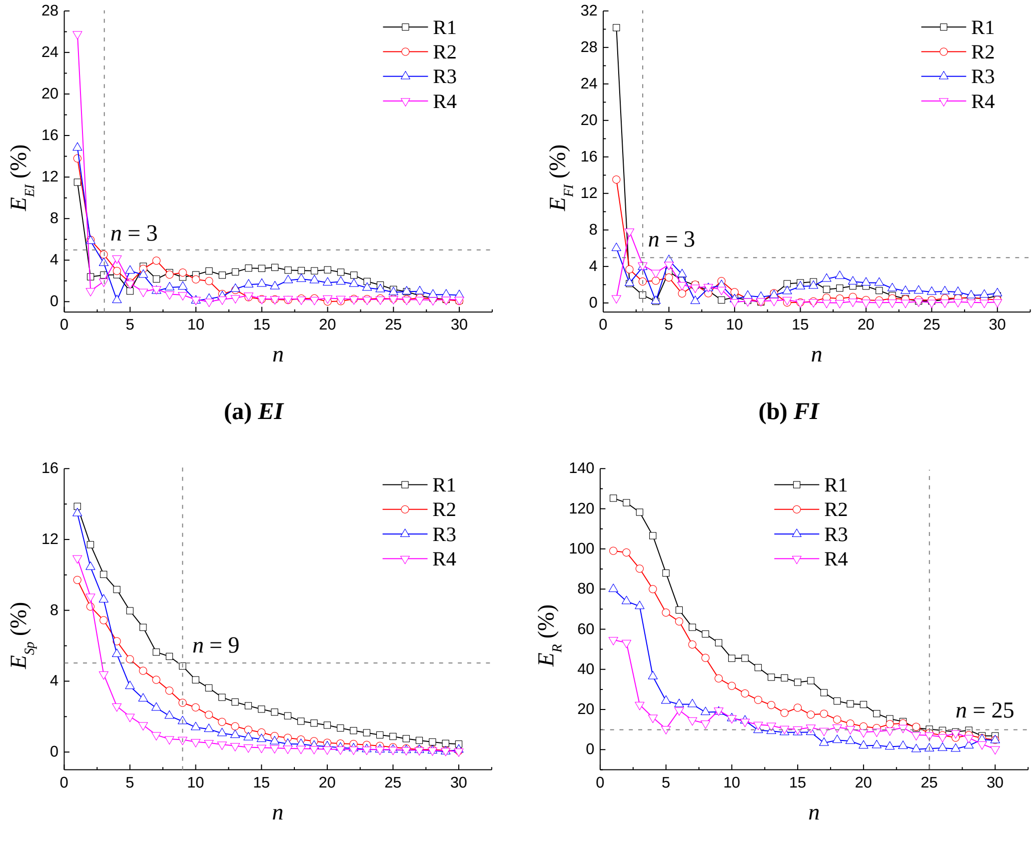

(a) ***EI*** (b) ***FI*** (c) $\boldsymbol{S_p}$ (d) ***R***

Fig. 10 Relationship between valued of *n* and relative errors of the morphological features of the SH reconstructed blocks

As shown in Fig. 10, the *EI* and *FI* of blocks reach a stable value for *n* values higher than 3, with E_{EI} and E_{FI} values both less than 5 %. Inspection of the figure reveals that S_p and *R* are more difficult to be described, necessitating a higher value of *n*, especially for blocks with the larger particle size. This is because these larger blocks are characterised by a larger angularity and more complex morphological details (see Figure 4c), indicating the description of the block surface with larger size needs more harmonics series than the smaller one. This is because The E_{Sp} of blocks are less than 5 % when *n* is higher than 9, while the E_R becomes lower than 10 % only for *n* higher than 25. As such, in order to describe accurately the morphological features of the SH reconstructed blocks, the value of n was fixed to 25 in the generation of SH series.

3.1.3 Generation of random SH series

Random SH series can be determined if a set of random SH coefficients a'^m_n are generated on the basis of the SH coefficients a^m_n obtained from the CT scanned blocks. Before the generation of a'^m_n, the CT reconstructed blocks were normalised to remove the influence of their initial orientations and volumes on the SH coefficients by (a) rotating them to have their principal axes parallel to the global coordinate axes; (b) scaling their volume to a unity.

N CT reconstructed blocks were selected as samples for establishing the random SH coefficients. N random numbers r_i, with sum equal to 1, were initially generated, producing the new normalised random SH coefficients a'^m_n:

$$a'^m_n = r_1\left(\overline{a^m_n}\right)_1 + r_2\left(\overline{a^m_n}\right)_2 + \cdots + r_i\left(\overline{a^m_n}\right)_i + \cdots + r_N\left(\overline{a^m_n}\right)_N \tag{16}$$

where $\left(\overline{a^m_n}\right)_i$ is the normalisation SH coefficients of the ith selected CT reconstructed block and $\sum_{i=1}^{N} r_i = 1$.

Following this procedure, thousands of normalised random blocks with unit volume can be established only by creating sets of random number.

3.1.4 Selection of available random blocks

The particle size of the normalised random blocks should be modified consistently with that of the real blocks. Accordingly, the same random number set r_i used in the generation of random SH coefficients was adopted to define the new particle size D' as follow:

$$D' = r_1 D_1 + r_2 D_2 + \cdots + r_i D_i + \cdots + r_N D_N \tag{17}$$

where D_i is the particle size of ith selected CT scanned block.

Although the random blocks were generated on the basis of the real blocks, some of them are characterised by morphological features not within the ranges identified by the real sampled blocks. For example, Fig. 11 compares the sampled blocks A and B with different random blocks, labelled as C1, C2, C3, C4 and C5.

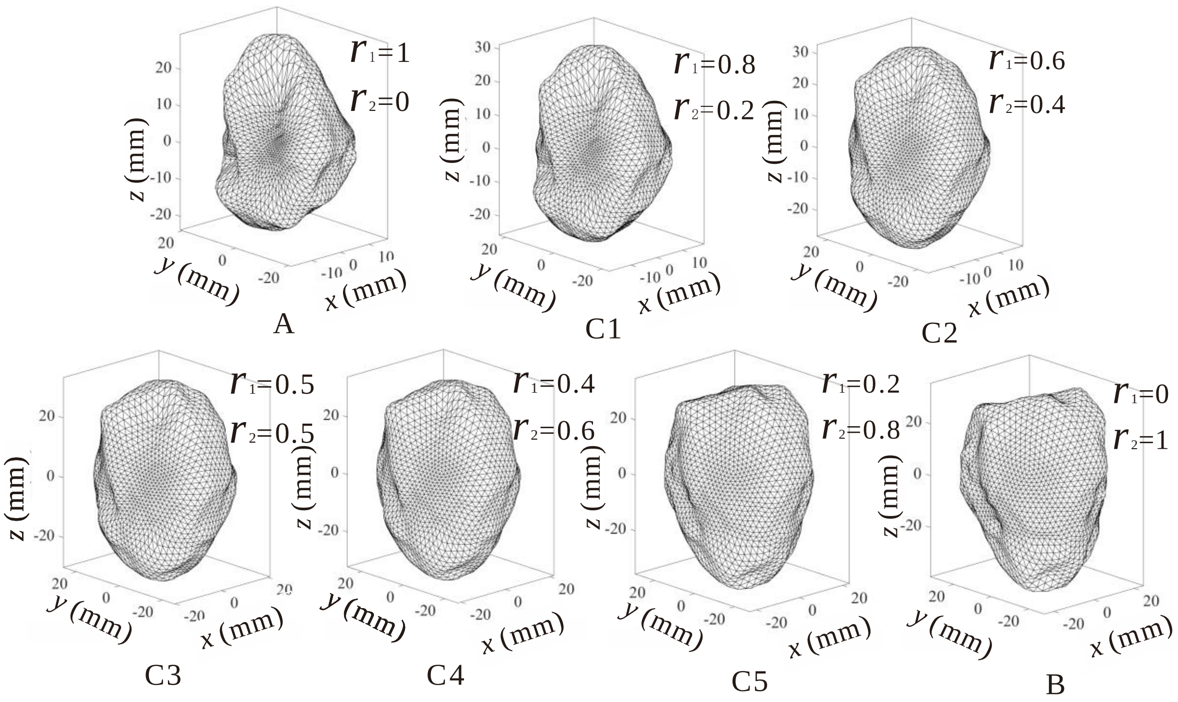

Fig. 11 Random generated blocks based on sample blocks A and B

Random blocks are more similar to block A when r_1 is larger or to block B when r_2 is. The morphological features of the generated blocks are summarised in Table. 1: it is evident that the S_P and R of C3 and C4 blocks are beyond the range of values identified by the sampled blocks A and B. As such, only the random blocks C1, C2 and C5 can be considered as available while C3 and C4 need to be disregarded.

The random blocks were considered as available for the next S-RM model generation only if their morphological features obeyed to all the rules given by Eq. (1), Eq. (3) and Eq. (6).

Table. 1 Morphological features of random blocks generated by block A and B

Block id	r_1	r_2	D (mm)	V (mm^3)	S (mm^2)	EI	FI	S_p	R
A	1.0	0.0	42.1	5395.4	27902.3	0.79	0.79	0.82	0.47
C1	0.8	0.2	45.9	6499.3	39475.6	0.80	0.80	0.86	0.50
C2	0.6	0.4	49.6	7750.9	54251.6	0.81	0.79	0.89	0.53
C3	0.5	0.5	53.4	9229.7	72792.8	0.81	0.81	0.91	0.54
C4	0.4	0.6	51.5	8478.5	63272.2	0.81	0.80	0.91	0.54
C5	0.2	0.8	57.2	10590.1	89733.1	0.81	0.81	0.92	0.53
B	0.0	1.0	61.0	11927.3	104028.5	0.82	0.81	0.90	0.53

3.2 Stochastic fracture generation approach

An example of CT fractures reconstructed in the block was given in Fig. 3b. Considering their complex 3D morphological features, difficult to be described precisely, simplified cubic stochastic fracture models were developed on the basis of their statistical characteristics.

3.2.1 Determination of fracture numbers

According to the statistical characteristics of real fractures, random fractures were generated only in the blocks having a particle size in the range 40 - 80 mm. The number of fractures N_{fi} in ith block can be simply determined by the block volume V_i considering the average fracture frequency of real fractures (i.e. 10^{-4} per 1 mm^3). As such, the total number of random fractures N_{ft} is:

$$N_{ft} = \sum_{i=1}^{M} N_{fi} = \sum_{i=1}^{M} \mathrm{INT}(V_i \times 10^{-4}) \tag{18}$$

where INT is a function that approximate the resulting value to the nearest integer. M is the number of blocks with size between 40 mm and 80 mm in the S-RM sample.

3.2.2 Determination of characteristics of random fractures

The relative orientations of random fractures were created on the basis of real ones. A set of random numbers θ_j ($1 \le j \le N_{ft}$) were generated to obey an Amplitude Gaussion distribution having the same mean μ and standard deviation σ of the θ distribution of scanned fractures. The offset y_0 and amplitude A were scaled on the basis of the number of scanned fractures N and generated random ones M in the S-RM sample. As such, the θ_j distribution reads:

$$F_f = \frac{M \times \left(26.8\text{-}1441.5 \bullet \frac{1}{\sqrt{2\pi} \bullet 22.7} e^{-\frac{(\theta-70.2)^2}{2 \bullet 22.7^2}} \right)}{N} \quad , \quad 0° \le \theta \le 180° \tag{19}$$

Similar to the process of generation of the random fracture orientations, the l_{fa} values of random fractures, ranging from 2 mm to 16 mm, were also created on the basis of the corresponding l_{fa} distribution of the scanned fractures, expressed in Eq. (7). Based on the l_{fa} distribution, a random l_{fa} set A_j was generated for representing the l_{fa} dimension of jth random fracture.

3.2.3 Determination of available l_{fb} and l_{fc}

Based on the l_{fb} dimension of scanned fractures, another set of number B_j was also randomly generated in the interval 1.5 - 12 for representing the l_{fb} dimension of jth random fracture. If the relationship between B_j and A_j was found to fit in the range indicated by the Eq. (8) valid for the corresponding l_{fb} and l_{fa}

dimensions, B_j was considered as an available random number; otherwise, a new random number was created until it conformed to this law. A similar procedure was adopted for the random generation of a series of C_j values in the interval from 0.7 to 8, representing the l_{fc} dimension of jth random fracture, ensuring that each value satisfied the limits imposed by Eq. (9) with respect to A_j.

3.3 Generation approach for block DEM models

The commercial software Particle Flow Code in three-dimensions (PFC^{3D}5.0) was employed to create blocks and S-RM DEM models. The cluster, used to simulate the block, consists of a group of bonded balls with a specified bond strength, commonly used to simulate breakable geomaterials with a certain strength. A cluster behaves as a deformable body, contact forces being generated and updated during the analysis; it breaks once its bond strength is reached. The block DEM model was generated following the next steps:

(a) ***Importing block and fractures geometries***. A block geometry generated by the stochastic block generation approach was imported and the necessary number of random fractures was determined. The fracture geometries were selected from the total M generated stochastic fractures and imported in the block. The spatial distribution of the fractures were assumed to be randomly distributed within the block; however, a regeneration step was performed if the fractures were found to intersect the surface of block (Fig. 12a).

(b) ***Generation of fracture balls***. Considering that the minimum size of the fractures are only 0.8 mm, the minmum radius of fracture balls were set as 8 times less than that of fractures. Balls with radius of 0.1 - 0.15 mm were generated in each fracture to fill it completly (Fig. 12b).

(c) ***Generation of block balls***. In order to reflect the block morphological features, the maximum radius of block balls were set as 10 times less than that of blocks. Block balls with a porosity of 0.35 were generated in the block without the position occupied by the fractures. After fixing all fracture balls, the boundaries of all the geometries were taken as the wall boundaries and the analysis was started until a balanced state was reached in the assembly (Fig. 12c).

(d) ***Generation of block cluster.*** After generating block balls, the fracture balls were all deleted and the block balls were fixed at their position. Then the block cluster model was finally generated by bonding the block balls with each others by a specified strength (Fig. 12d).

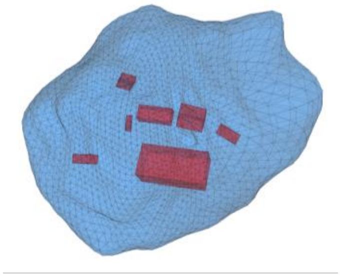

(a) Importing geometries of blocks and fractures

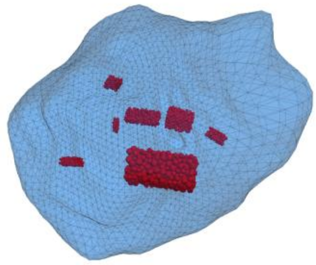

(b) Generation of fracture balls

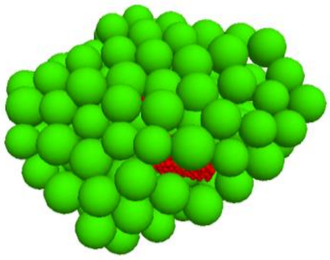

(c) Generation of block balls

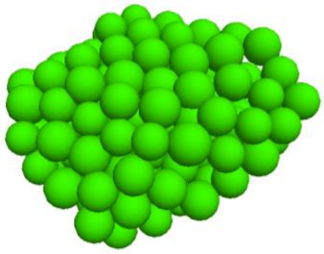

(d) Generation of block cluster

Fig. 12 Generation process of the block DEM model

4 Generation of 3D random S-RM DEM models

The *VBP* of the investigated S-RM samples, introduced in Section 2.1, was in the range of 35% - 60%. In particular, the numerical approach will be developed with reference to a S-RM sample characterised by a *VBP* of 40%, for which the results of a large direct shear test are available for the sake of comparison.

4.1 Generation of block assembly

Based on the grain size distribution of rock blocks identified experimentally, a total number of 4085 random blocks was generated following the proposed stochastic block generation approach (Table 2). Similarly, 2335 random fractures were also created for blocks with size of 40 - 80 mm.

Table. 2 Generated rock blocks according to different stes of size dimension

Block Size	10 - 20 mm	20 - 40 mm	40 - 60 mm	60 - 80 mm
VBP (%)	3.1	12.5	14.4	10
Volume (mm^3)	3077200	12308800	14155120	9847040
Number	3100	702	198	85

The block DEM assembly was generated following two steps (Fig. 13a): (a) first, the shear box employed in the laboratory tests, consisting of a cylinder with a diameter of 560 mm and a height of 400 mm, was introduced; (b) then, the generated block DEM models were imported in the shear box one by one with random spatial and orientation distributions. In order to avoid block overlapping, the block models were set as independent clumps, separated later after some calculation steps.

4.2 Generation of S-RM models

In the S-RM sample, particles with size lower than 10 mm are considered as soil particles (i.e. matrix). Considering of the limitation of the computation capacity, the soil particles were simplified as sphere balls having radii from 4.8 mm to 5.0 mm for representing the soil particles in the DEM model. Although the morphology of soil particles can be represented by bonding several smaller balls, this will lead to a large increase in the particle number in the DEM model. As such, the irregular morphology of soil particles was neglected and the rolling resistant model was adopted for simulating their roughness (Jiang et al. 2005, Xu et al. 2016b).

However, the generated soil balls were characterised by a large overlap within the block clumps. The maximum degree of overlap O_i of ith soil ball with the surrounding balls in the block clumps can be expressed as follow:

$$O_i = max(1-\frac{D_{sb}}{r_{si}+r_{bj}})\times 100\% \quad (j = 1,2,....,N_{cb}) \tag{20}$$

where D_{sb} is the distance from the centre of ith soil ball to that of jth block ball. r_{si} and r_{bj} are the radii of ith soil ball and jth block ball, respectively. N_{cb} is the total number of clump balls in the S-RM model. Soil balls with a O_i larger than a selected threshold (e.g. 10 %, 20 %, 30 %, 40 %, 50 %, 60 %, 70 %, 75 %, 80 % and 90 %) were then deleted from the model and the porosity of the S-RM sample was recalculted after balancing the model. As shown in Fig. 13b, after deleting the soil balls with O_i larger than 75%, the porosity of the S-RM sample reached the required value, equal to 0.38.The final resulting 3D S-RM DEM model with 40% *VBP* was then established by transferring the block clumps into clusters and bonding the balls in the clumps with a specified strength value (Fig. 13c).

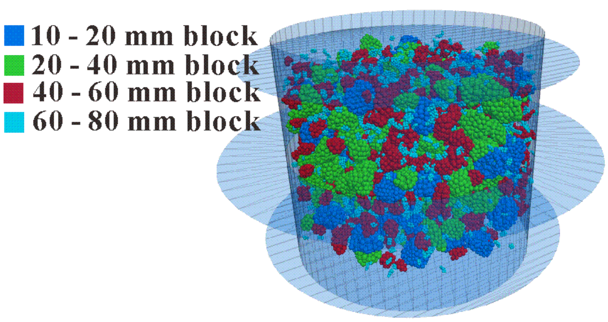

(a) Generated blocks assembly

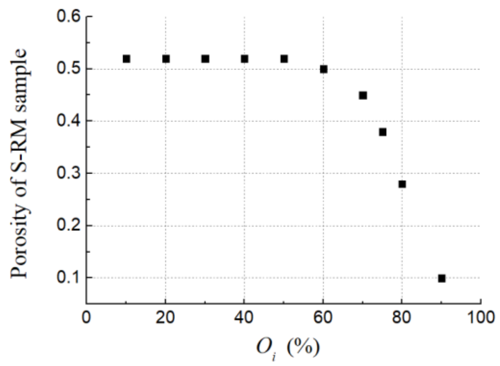

(b) The sample porosity after deleting balls with O_i larger than specified values

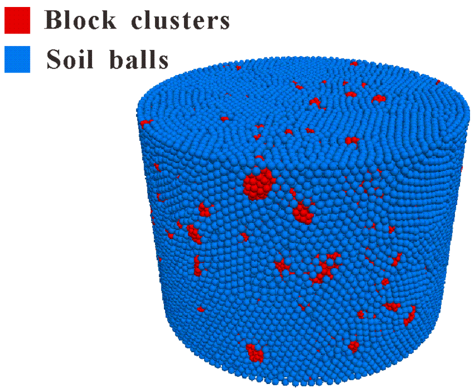

(c) Generated S-RM DEM model

Fig. 13 Generation process of S-RM DEM model

The block morphological features and fracture characteristic distributions of the generated S-RM DEM model are provided in Fig. 14, demonstrating that thousands of random blocks and fractures can be reasonably produced for generating S-RM models on the basis of a limited number of scanned blocks and fractures using the proposed stochastic generation approaches.

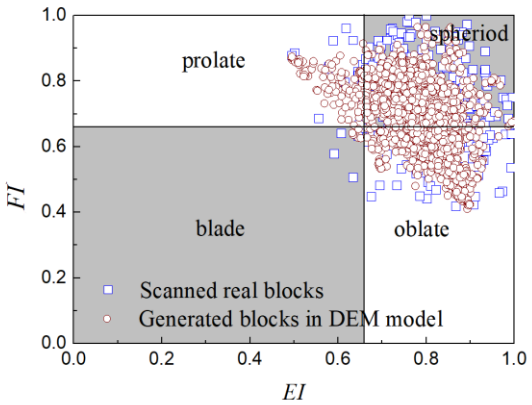

(a) *EI* and *FI* of blocks

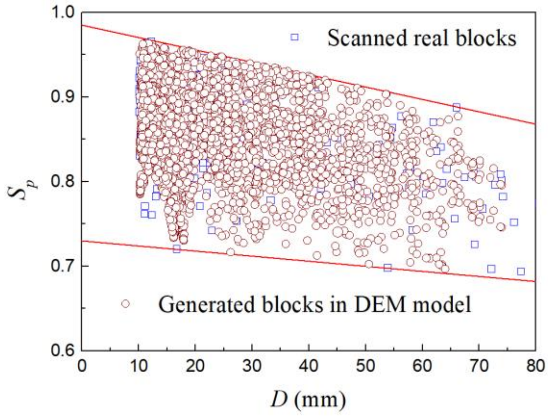

(b) Sphericity of blocks

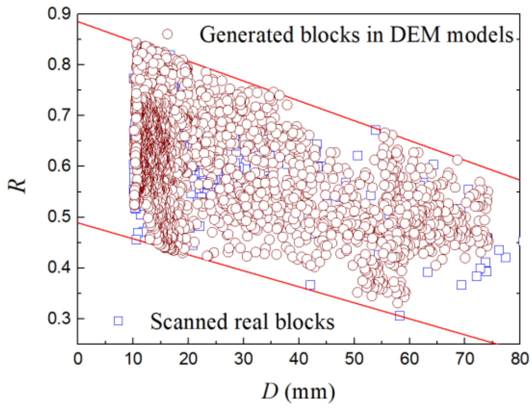

(c) Roundness of blocks

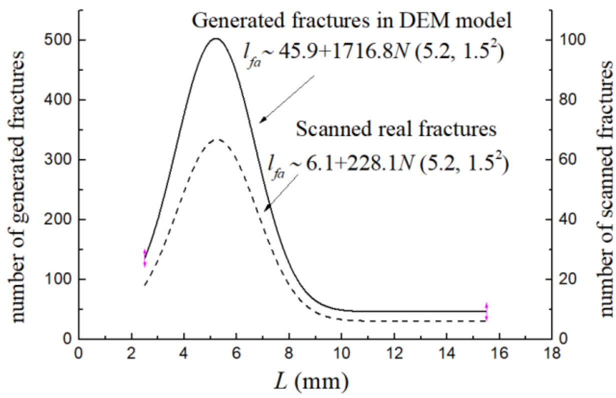

(d) l_{fa} distribution of fractures

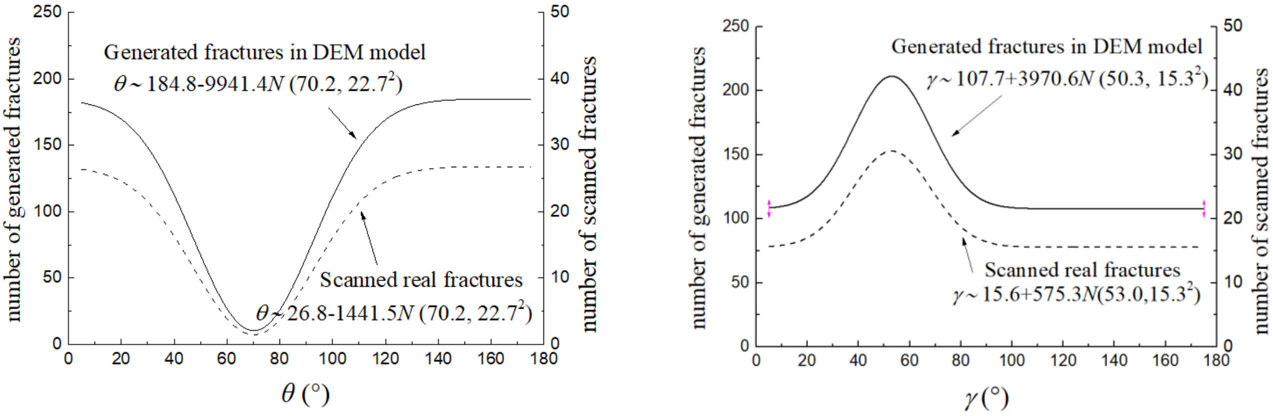

(e) θ distribution of fractures **(f) γ distribution of fractures**

Fig. 14 Morphological and fractures characteristics of scanned blocks and generated blocks in the DEM model

4.3 Determination of meso-parameters

Macro-mechanical properties (e.g. elasticity modulus, cohesion and friction angle) of DEM models are commonly represented by the meso-parameters of particles (e.g. stiffness, friction coefficient and bond strength). Rolling resistant model was adopted for simulating the soil mechanical behaviours, while the parallel bond model was used to represent the mechanical behaviour of breakable blocks.

4.3.1 Meso-parameters of soil particles

To obtain the meso-mechanical parameters of the S-RM matrix, particles with diameter less than 10 mm were sieved from the S-RMs to perform large laboratory DSTs. During the tests, the applied normal stresses were 100 kPa, 200 kPa, 300 kPa, 400 kPa and 500 kPa.

About 78,000 soil particles with radius of 4.8 mm - 5 mm were generated in a DEM model having the same size of the large soil DST, and numerical tests were performed under the same normal stresses. The parameters of soil particles used in the DEM simulations are summarised in Table 3.

Inspection of Fig. 15a reveals a very good match between experimental and numerical shear stress - shear displacement curves. Interpretation of numerical results provided a cohesion and friction angle respectively equal to 21.4 kPa and 29.6 °, very close to the values obtained from laboratory tests, namely 20.8 kPa and 29.6°. As such, it was demonstrated that the meso-parameters selected for the soil particles are appropriate for representing the soil mechanical behaviours in DEM simulations.

4.3.2 Meso-parameters of block clusters

To obtain the meso-parameters of block clusters right on the basis of the block geometries, one CT scanned block with a particle size of 64 mm was selected for performing an uniaxial compression test using a servo test system (Fig. 15b). In particular, an axial displacement rate of 0.002mm/s was adopted.

The same test was simulated numerically on a block cluster, generated considering the geometry of the tested block and having internal fractures with the meso-parameters given in Table 3 (Fig. 15c). Fig. 15d shows the good agreement between the numerical and experimental simulations, indicating that the selected meso-parameters allow to well reproduce the mechanical behaviour of blocks.

In the S-RM model, the contacts between the soil and block particles obey to a rolling resistance model. The meso-parameters of the contacts between soils and blocks are summarised in Table 3.

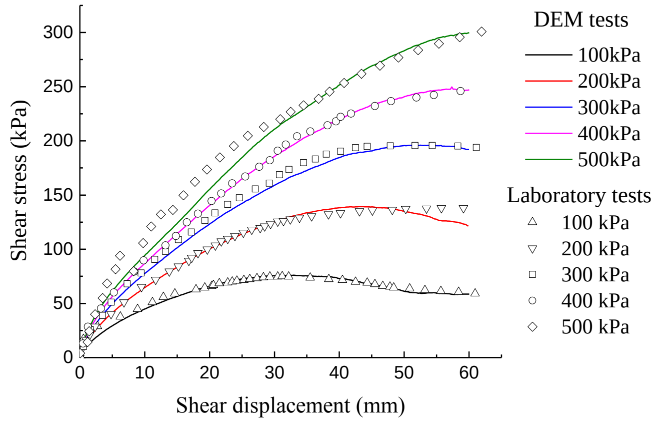

(a) Shear stress vs. shear displacement curves of soil laboratory tests and DEM tests under different normal stress

(b) Laboratory unaxial compression test of single block

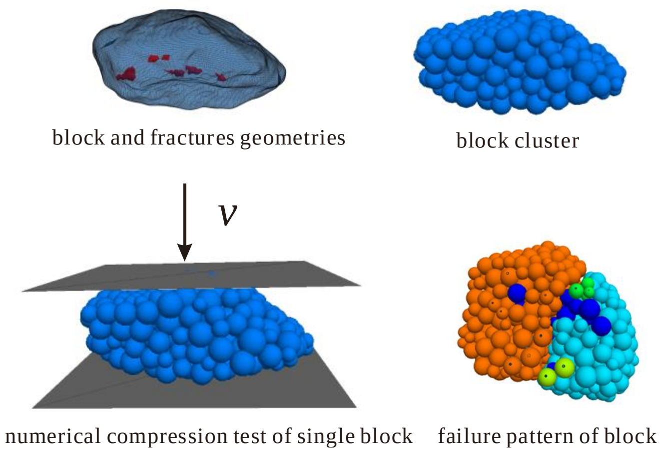

(c) DEM unaxial compression test of single block

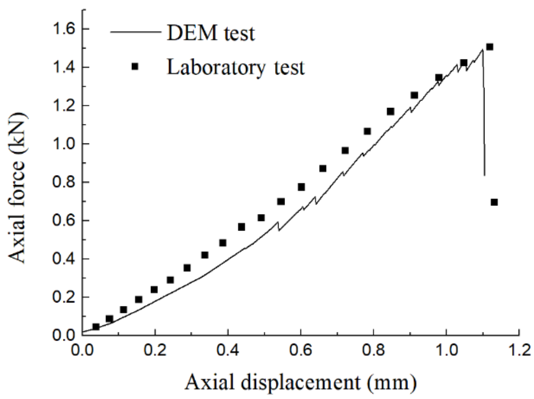

(d) Axial force vs. axial displacement of laboratory and DEM compression test of single block

Fig. 15 Laboratory and DEM tests of soil and single block

Table 3 Meso-parameters of materials used in S-RM models

Material	Parameter	Value
Soil particles	Density of particles (kg/m^3)	1850
	Damp of particles	0.2
	Elastic modulus of particle contacts (MPa)	10.0
	Poisson’s ratio of particle contacts	0.5
	Friction coefficient	0.5
	Rolling resistance coefficient	0.05
Block particles	Density of particles (kg/m^3)	2500
	Damp of particles	0.2
	Elastic modulus of particle contacts (MPa)	110.0
	Poisson’s ratio of particle contacts	0.5
	Friction coefficient	0.65
	Bond tensile strength (MPa)	1.5
	Bond shear strength (MPa)	1.5
Contacts between soil and blocks particles	Elastic modulus of contacts (MPa)	110.0
	Poisson’s ratio of contacts	0.5
	Friction coefficient	0.65
	Rolling resistance coefficient	0.10

5 S-RM numerical tests

5.1 Numerical direct shear tests

5.1.1 Simulation process

Direct shear tests performed in laboratory ((i.e. with normal stresses of 100 kPa, 200 kPa, 300 kPa, 400 kPa and 500 kPa) were simulated consistently with the generated DEM sample. This latter was initially consolidated under the specified normal stress, by controlling the velocity of the top wall of the shear box until the applied normal stress reached the target value. Then, shear loading was applied by moving horizontally the upper shear box wall, with a displacement rate of 0.1 mm/s, slow enough to ensure the sample remains in quasi-static equilibrium (i.e. Cho et al, 2008), while fixing the lower one. When the horizontal displacement reached 56 mm (i.e. 10% of shear strain), the shear test was considered as concluded.

During the shearing, the shear stress, normal stress and horizontal and vertical displacements were monitored and recorded automatically, as well as the number of meso-cracks, corresponding to the rupture of the bond between the block particles.

5.1.2 Numerical tests results

The shear stress - horizontal displacement curves of DEM and laboratory tests are compared in Fig. 16a. Before the peak strength, experiments and simulations were found to be in close agreement. However, the reduction in shear strenght was more pronounced in the DEM tests, possibly because a large number of blocks only broke after the peak value and the resulting fragments, being spherical, have a lower angularity than that of the real material.

As shown in Fig. 19b, when the applied normal stress was lower than 200 kPa, dilation occurred during the shearing stage, while the pattern changed from contraction to dilation for normal stresses higher than 300 kPa. The number of meso-cracks generated in the blocks increased rapidly with the horizontal displacement, the process being more pronounced for higher applied normal stresses (Fig. 19c).

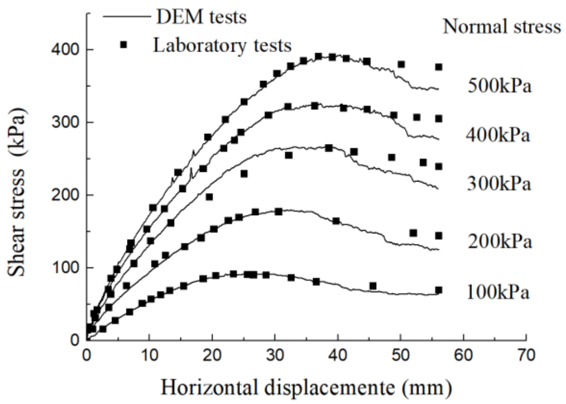

(a) Shear stress-horizontal displacement curves of DEM tests and laboratory tests

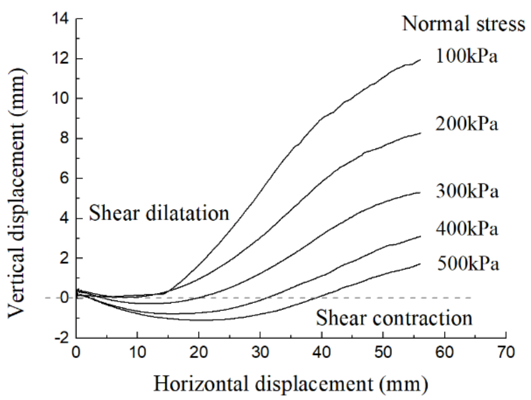

(b) Relationship curves of vertical and horizontal displacement curves of DEM tests

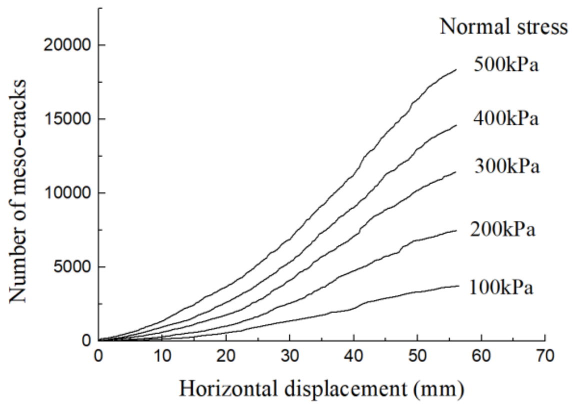

(c) Development of number of meso-cracks with horizontal displacement of DEM tests

Fig. 16 Tests results of DEM tests and laboratory tests under different normal stress

5.2 Evolution of S-RM deformation and failure processes

As shown in Fig. 17, the evolution of S-RM deformation and failure processes can be divided into three stages: the compaction stage, the yield stage and the failure stage. The three stages are described as follows.

(a) Compaction stage (stage O-A)

With the increase in horizontal displacement, the vertical contraction increased and attained the peak value when the horizontal displacement reached point A (Fig. 17a). The rate of shear stress increment had a small reduction, owing to a small amount of meso-cracks, mainly caused by tensile forces, generated in the S-RM sample (Fig. 17b). The few generated meso-cracks were found to be scatteredly distributed in the S-RM sample, and no broken blocks were still observed at this stage (Fig. 18a).

When horizontal displacement reached point A, only some soil paricles close to the lateral shear box rotated (Fig. 18a), indicating that the shear surface began to develop along the rotated soil particles from the upper right and lower left corner of shear box.

(b) Yield stage (stage A-B)

During this stage, the rate of shear stress increment experienced a significative reduction, and a large number of meso-cracks, especially tensile ones, generated in the blocks. Peak strength was attained at point B: as shown in Fig. 18b, some blocks in the centre of the sample displayed an obvious rotation, producing a change in the vertical displacement from contraction to dilation.

A localization band was observed from the rotation distribution of the particles (Fig. 18b). In addition, some rotated blocks were broken at this stage, indicating that shear surfaces started developing, from the lateral sides of the shear box to it centre, and connecting, by rounding the blocks or even penetrating through them.. The localization band formed with vertical thickness of 9.8 mm.

(c) Failure stage (stage B-C)

The failure stage was characterised by a decrease in the shear stress after the peak related to the large number of meso-cracks and the breakage of blocks. Many blocks in the centre of sample were subjected to a large rotation, producing a further dilation of the S-RM sample.

The rotated blocks and soil particles distributed in the centre of sample with a larger vertical thickness of 13.2 mm when the displacement reached point C, characterised by a well developed localization band (Fig. 18c).

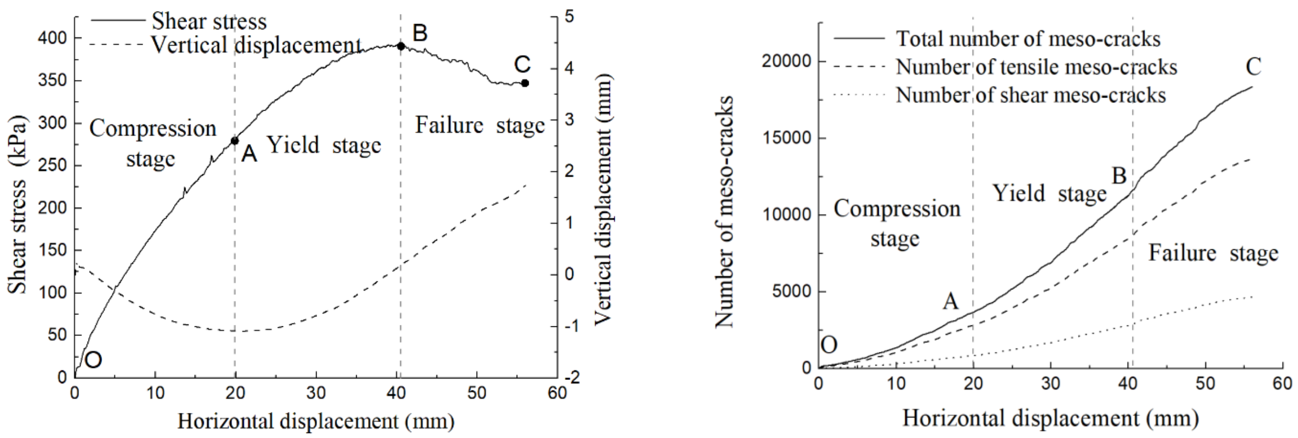

(a) Evolution of shear stress and vertical displacement **(b) Evolution of meso-cracks number**

Fig. 17 Evolution of shear stress, vertical displacement and meso-cracks number of S-RM sample under 500kPa normal stress

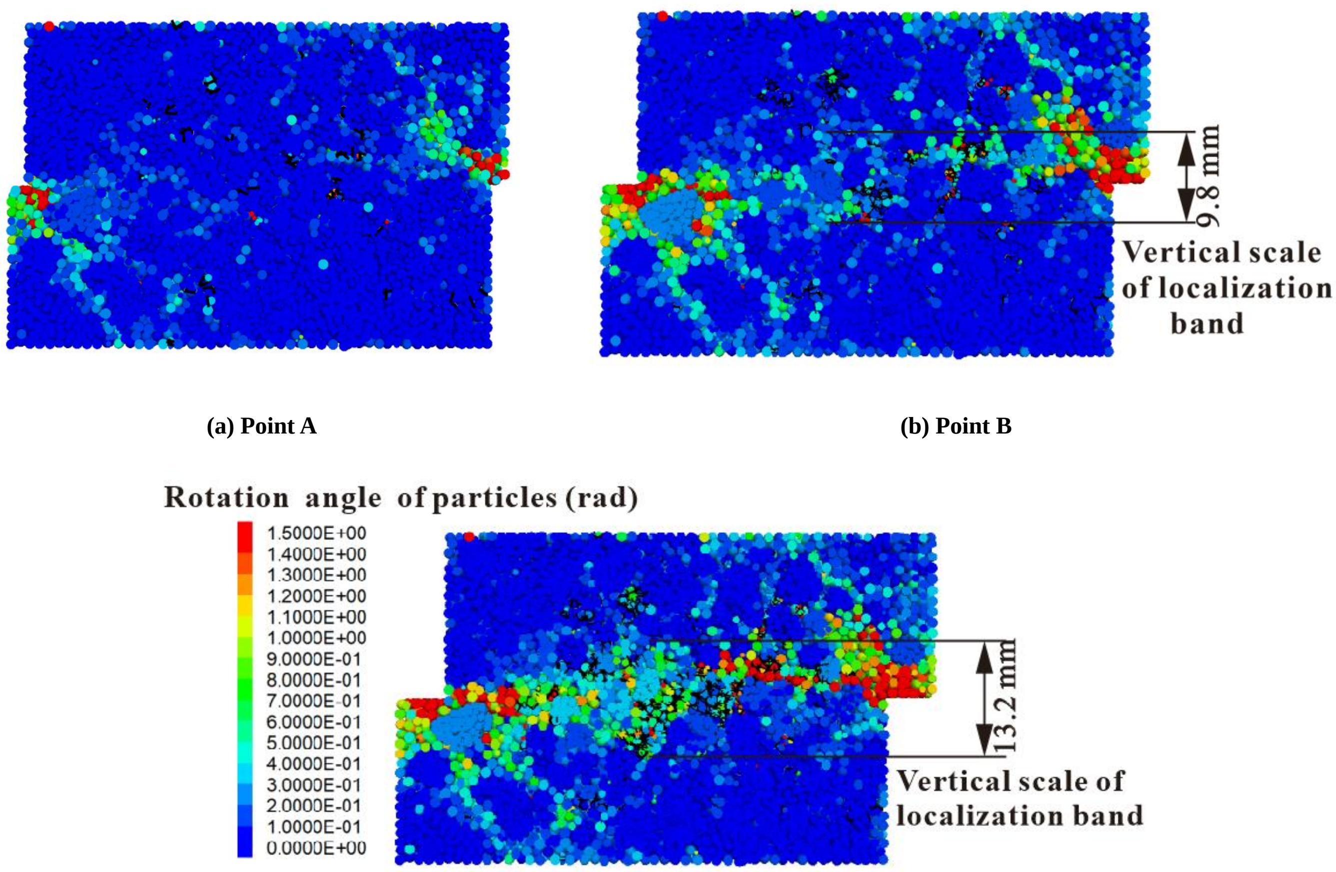

(a) Point A **(b) Point B**

(c) Point C

Fig. 18 Evolution of particle rotation and meso-cracks in the middle section of S-RM model under 500kPa normal stress

(the rotation angle is clockwise angle of particles; the black short solid lines are the generated meso-cracks in the blocks)

5.3 Shear strength of S-RM

In order to analyse the influence of the block breakage and the presence of internal fractures on the shear strength of S-RMs, two new sets of S-RM models were created : (i) S-RM models with unbreakable blocks, generated by replacing the block clusters with block clumps (see Table 4), with the same soil meso-parameters of original ones; (ii) S-RM models with breakable blocks but without internal fractures, adopting the same meso-parameters of soil and block clusters of the original S-RM models.

Table 4 Meso-parameters of block clumps used in S-RM models with unbreakable blocks

Parameter	Value
Density of clumps (kg/m^3)	2500
Damp of particles	0.2
Elastic modulus of clump contacts (MPa)	110.0
Poisson's ratio of clump contacts	0.5
Friction coefficient	0.65
Rolling resistance coefficient	0.10

The shear strength resulting from the two new sets of simulations is compared to the original one in Fig. 19. As expected, the shear strength of the unbreakable S-RM samples was the highest one, indicating the role played by breakable blocks, especially at high normal stresses. Consideration of internal fractures in the breakable S-RM significantly reduced the shear strength of breakable S-RM, demonstrating the importance of this feature in the S-RM modelling.

It was also found that neglecting the possible block breakage and the presence of internal fractures strongly affects the calculated strength parameters of the S-RM. The cohesion c of unbreakable S-RM samples was lower than that of the breakable ones while its friction angle φ was higher. A similar trend was observed in those models not accounting for the presence of internal fractures.

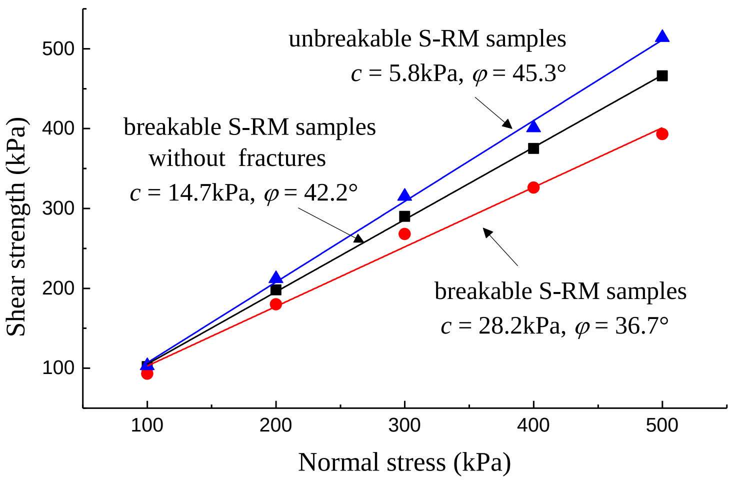

Fig. 19 Shear strength of breakable and unbreakable S-RM samples

Conclusions

This study proposes stochastic approaches for generating block and fracture models, accounting for morphological features and internal fracture characteristics of breakable blocks, to be adopted in the setting up of 3D S-RM DEM models.

The research takes its cue from the case-history of an artificial S-RM filling slope, mainly containing highly-weathered shale blocks, located in the Funing County, Yunnan Province, China. The 3D morphological features of shale blocks and the characteristics of their internal fractures were obtained by CT technology and image processing. Stochastic block generation methods were developed on the basis of SH series of real blocks for establishing random blocks DEM cluster models. Similarly, random fracture models, simulated as voids in the block clusters, were created by a stochastic generation approach on the basis of real fracture characteristic distributions. The attention was focused on a 3D modelling of a S-RM with 40% *VBP*, by setting reasonable meso-parameters. Its mechanical behaviour during numerical direct shear tests was analysed in detail, to investigate the mechanisms of shear band development and localisation and the role played by block breakage and internal fractures.

The following main conclusions can be drawn:

(1) The shale blocks were mainly spheroidal and their sphericity was found to be in the range of 0.7 - 0.97, typically larger for the smaller blocks. The roundness of blocks varied from 0.3 - 0.8, the larger blocks having a higher angularity than the smaller ones. The average frequency of real fractures was 0.1 per $1\,\mathrm{cm}^3$ in the blocks with size of 40 - 80 mm. The size and orientation distributions of fractures were both found to obey the Amplitude Gaussian laws.

(2) In the random block generation approach, the SH degree of blocks *n* was accurately determined on the basis of the block morphological features, fixed to 25 for the generation of random SH series. The distributions of random fracture sizes and orientations were also reasonably determined on the basis of those of real fractures. Thousand random blocks and fractures with similar morphological features and characteristic distributions to real ones were produced in the S-RM DEM models using the developed stochastic block generation approach.

(3) The comparison between the results of DEM and laboratory direct shear tests demonstrated that the generated random S-RM DEM models and the selected meo-parameters can be reasonably used for reproducing the mechanical behaviour of S-RM samples with breakage blocks.

(4) The evolution of S-RM shearing process can be subdivided into three stages: the compaction stage, the yield stage and the failure stage. The shear surface formed from the lateral shear box to the centre of sample during the compaction stage; then it connected by rounding the blocks or even penetrating through them, producing a localization band with rotated blocks in the yield stage; finally, the localization band developed with a larger vertical scale at the failure stage. The breakage of blocks mainly occured in the localization band, mostly casued by tensile forces.

(5) It was also demonstrated that neglecting block breakage and the presence of internal fractures had significant influence on the shear strength of the S-RM model, by increasing its shear strength and friction angle while reducing its cohesion.

The stochastic generation approach can be also used for establishing other S-RM samples with different block morphological features, block volume proportions and fracture distributions. The influence of all these factors on the S-RM mechanical behaviour is the object of future research.

Acknowledgements

This study is funded by the Key Program of National Natural Science Foundation of China (41630643), and the Fundamental Research Funds for the Central Universities, China University of Geosciences (Wuhan) (Nos. CUGCJ1701, 1810491A26).

Reference

Barrett PJ (1980) The shape of rock particles, a critical review. Sedimentology 27(3), 291 - 303. https://doi.org/10.1111/j.1365-3091.1980.tb01179.x.

Bullard JW, Garboczi EJ (2013) Defining shape measures for 3D star-shaped particles: Sphericity, roundness, and dimensions. Powder Technology 249: 241-252. https://doi.org/10.1016/j.powtec.2013.08.015

Coli N, Berry P, Boldini D (2011) In situ non-conventional shear tests for the mechanical characterisation of abimrock. International Journal of Rock Mechanics and Mining Sciences 48(1): 95-102. https://doi.org/10.1016/j.ijrmms.2010.09.012.

Coli N, Boldini D, Bandini A, Lopes DS (2012, May 28) Modeling of complex geological rock mixtures under triaxial testing conditions. ISRM International Symposium - EUROCK 2012, Stockholm, Sweden, International Society for Rock Mechanics and Rock Engineering: 12.

Cheng GW, He JM, Li X, Di BR, Li SD (2010) Particle Flow Simulation for Soil-rock Mixtures under BiaxialPressure. Mining and Metallurgical Engineering, 30(4): 1-4,8. [in Chinese] https://doi.org/10.3969/j.issn.0253-6099.2010.04.001.

Cheng Z, Wang J (2018a) Experimental investigation of inter-particle contact evolution of sheared granular materials using X-ray micro-tomography. Soils and Foundations, 58(6): 1492-1510. https://doi.org/10.1016/j.sandf.2018.08.008.

Cheng Z, Wang J (2018b) A particle-tracking method for experimental investigation of kinematics of sand particles under triaxial compression. Powder Technology, 328(1): 436-451. https://doi.org/10.1016/j.powtec.2017.12.071

Calseira LMMS, Brito A (2014) Use of soil-rock mixtures in dam construction. Journal of Construction Engineering and Management 140(8): 04014030. https://doi.org/10.1061/(asce)co.1943-7862.0000864.

Chen L, Yang YT, Zheng H (2018) Numerical study of soil-rock mixture: generation of random aggregate structure. Science China Technological Sciences, 061(003): 359-369. https://doi.org/10.1007/s11431-017-9136-9

Cen D, Huang D, Ren F (2017) Shear deformation and strength of the interphase between the soil-rock mixture and the benched bedrock slope surface. Acta Geotechnica 12(2): 391-413. https://doi.org/10.1007/s11440-016-0468-2.

Dong Y (2007) Experimental study on intensity character of rock-soil aggregate mixture. Rock and Soil Mechanics 38(1): 1260-1274. [in Chinese] https://doi.org/10.1007/s11747-006-0011-3.

Fonseca J, O'Sullivan C, Coop MR, Lee PD (2012) Non-invasive characterization of particle morphology of natural sands. Soils Found 52 (4): 712 - 722. https://doi.org/ 10.1016/j.sandf.2012.07.011.

Fu R, Hu XL, Zhou B, Wang HB, Wang JF (2018) A quantitative characterization method of 3D morphology of sand particles. Rock and Soil Mechanics 39(2): 483 - 490. [in Chinese] https://doi.org /10.16285/j.rsm.2017.1825.

Feng ZK, Xu WJ, L R (2020) Three-dimensional morphological characteristics of particles in nature and its application for DEM simulation. Powder Technology 364: 635-646. https://doi.org/10.1016/j.powtec.2020.02.022.

Garboczi EJ (2002) Three-dimensional mathematical analysis of particle shape using X-ray tomography and spherical harmonics: application to aggregates used in concrete. Cement and Concrete Research 32(10): 1621 - 1638. https://doi.org/ 10.1016/S0008-8846(02)00836-0.

Hamidi A, Salimi N, Yazdanjou V (2011) Shape and size effects of gravel particles on shear strength characteristics of sandy soils. Geosciences 20(80): 189-196. https://doi.org/10.1201/9780203885284-c50.

Hu XL, Zhang H, He CC, Zheng WB (2018) Breakage Effect of Soft Rock Blocks in Soil-Rock Mixture with Different Block Proportions. In: Proceedings of China-Europe Conference on Geotechnical Engineering, Springer, Cham, pp. 809-813. https://doi.org/10.1007/978-3-319-97112-4_181.

ISO (2008) ISO 9276 - 6: 2008: Representation of results of particle size analysis - Part 6: Descriptive and quantitative representation of particle shape and morphology. Geneva, Switzerland: ISO.

Jiang M, Yu H, Harris D (2005) Novel discrete model for granular material incorporating rolling resistance. Computers and Geotechnics 32(5): 340 - 357. https://doi.org/10.1016/j.compgeo.2005.05.001.

Kolyukhin D, Tveranger J (2014) Statistical analysis of fracture-length distribution sampled under the truncation and censoring effects. Mathematical Geosciences 46(6): 733-746. https://doi.org/10.1007/s11004-013-9517-7.

Li X, Liao QL, He JM (2004) In-situ tests and a stochastic structural model of rock and soil aggregate in the three Gorges Reservoir area, China. International Journal of Rock Mechanics and Mining Sciences 41(3):702–707. https://doi.org/10.1016/j.ijrmms.2004.03.122.

Liu XR, Tu YL, Wang LF, Feng H, Zhong ZL, Lei XD, Wang L (2017) Fractal characteristics of shear failure surface and mechanism of strength generation of soil-rock aggregate. Chinese Journal of Rock Mechanics and Engineering 36(9): 2260-2274. [in Chinese]. https://doi.org/10.13722/j.cnki.jrme.2016.0967.

Liang YJ (2016) Rock fracture skeleton tracing by image processing and quantitative analysis by geometry features. Journal of Geophysics and Engineering 13(3): 273 - 284. https://doi.org/10.1088/1742-2132/13/3/273.

Medley EW (1994) The engineering characterization of mélanges and similar block-in-matrix rocks (bimrocks). PhD thesis, Department of Civil Engineering, University of California, Berkeley, California.

Masad E, Saadeh S, Al-Rousan T, Garboczi E, Little D (2005) Computations of particle surface characteristics using optical and X-ray ct images. Computational Materials Science 34(4): 406 - 424. https://doi.org/10.1016/j.commatsci.2005.01.010.

Sonmez H, Gokceoglu C, Medley EW, Tuncay E, Nefeslioglu HA (2006) Estimating the uniaxial compressive strength of a volcanic bimrock. International Journal of Rock Mechanics and Mining Sciences, 43(4): 554-561. https://doi.org/10.1016/j.ijrmms.2005.09.014

Su D, Yan WM (2018) 3D characterization of general-shape sand particles using microfocus X-ray computed tomography and spherical harmonic functions, and particle regeneration using multivariate random vector. Powder Technology 323(1): 8 - 23. https://doi.org/10.1016/j.powtec.2017.09.030.

Wadell H (1932) Volume, shape and roundness of rock particles. J. Geol. 40(5): 443 - 451. https://doi.org/10.1086/623964.

Wu MM, Wang JF, Russell A, Cheng Z (2020) DEM modelling of mini-triaxial test based on one-to-one mapping of sand particles. Géotechnique, 1 - 49. https://doi.org/10.1680/jgeot.19.P.212.

Xu WJ (2008) Study on meso-structural mechanics (M-SM) characteristics and stability of slope of soil-rock mixtures (S-RM). PhD thesis, Institute of Geology and Geophysics, Chinese Academy of Science, Beijing [in Chinese].

Xu WJ, Hu RL, Tan RJ (2007). Some geomechanical properties of soil-rock mixtures in the Hutiao Gorge area, China. Geotechnique 57(3): 255-264. https://doi.org/10.1680/geot.2007.57.3.255.

Xu WJ, Hu LM, Gao W (2016a) Random generation of the meso-structure of a soil-rock mixture and its application in the study of the mechanical behavior in a landslide dam. International Journal of Rock Mechanics and Mining Sciences 86: 166-178. https://doi.org/10.1016/j.ijrmms.2016.04.007.

Xu WJ, Wang S, Zhang HY, Zhang ZL (2016b) Discrete element modelling of a soil-rock mixture used in an embankment dam. International Journal of Rock Mechanics and Mining Sciences 86: 141-156. https://doi.org/10.1016/j.ijrmms.2016.04.004.

Xu WJ, Xu Q, Hu RL (2011) Study on the shear strength of soil–rock mixture by large scale direct shear test. International Journal of Rock Mechanics and Mining Sciences 48(8): 1235-1247. https://doi.org/10.1016/j.ijrmms.2011.09.018.

Xu WJ, Yue ZQ, Hu RL (2008) Study on the mesostructure and mesomechanical characteristics of the soil-rock mixture using digital image processing based finite element method. International Journal of Rock Mechanics and Mining Sciences 45(5): 749-762. https://doi.org/10.1016/j.ijrmms.2007.09.003.

Xu WJ, Liu GY, Yang H (2020) Study on the mechanical behavior of sands using 3d discrete element method with realistic particle models. Acta Geotechnica 1-16 . https://doi.org/10.1007/s11440-020-00982-0.

Yue ZQ, Chen S, Tham LG (2003) Finite element modeling of geomaterials using digital image processing. Computers and Geotechnics, 30(5): 375-397. https://doi.org/10.1016/s0266-352x(03)00015-6.

Yang YT, Sun YH, Sun GH, Zheng H (2019) Sequential excavation analysis of soil-rock-mixture slopes using an improved numerical manifold method with multiple layers of mathematical cover systems. Engineering Geology 261(1): 1-13. https://doi.org/10.1016/j.enggeo.2019.105278.

Zheng J, Hryciw RD. (2015) Traditional soil particle sphericity, roundness and surface roughness by computational geometry. Geotechnique 65(6): 494 - 506. https://doi.org/10.1680/geot.14.P.192.

Zhao B, Wang J, Coop MR, Viggiani G, Jiang M (2015) An investigation of single sand particle fracture using X-ray micro-tomography. Geotechnique, 65(8), 625 - 641. https://doi.org/0.1680/geot.4.P.157.

Zhou B, Wang J, Zhao B (2015) Micromorphology characterization and reconstruction of sand particles using micro X-ray tomography and spherical harmonics. Engineering Geology 184(14): 126 - 137. https://doi.org/10.1016/ j.enggeo.2014.11.009.

Zhou B, Wang J. (2016) Generation of a realistic 3D sand assembly using X-ray micro-computed tomography and spherical harmonic-based principal component analysis. International Journal for Numerical and Analytical Methods in Geomechanics 41(1):93 - 109. https://doi.org/10.1002/nag.2548.

Zhou B, Wang J, Wang H (2017) Three-dimensional sphericity, roundness and fractal dimension of sand particles. Géotechnique 68(1): 1-13. https://doi.org/10.1680/jgeot.16.p.207.

Zhang H, Hu XL, Boldini D, He CC, Liu C, Ai CJ (2020) Evaluation of the shear strength parameters of a compacted S-RM fill using improved 2-D and 3-D limit equilibrium methods. Engineering Geology 269: 105550. https://doi.org/10.1016/j.enggeo.2020.105550.

Zhang ZL, Xu WJ, Xia W, Zhang HY (2016) Large-scale in situ test for mechanical characterization of soil-rock mixture used in an embankment dam. International Journal of Rock Mechanics and Mining Sciences 86: 317-322. https://doi.org/10.1016/j.ijrmms.2015.04.001.

Author Statement

The all authors' individual contributions are as follows:

Xinli Hu: Project administration, Funding acquisition, Supervision;

Han Zhang: Conceptualization, Methodology, Software; formal analysis, Data Curation, Investigation, Resources and Writing- Original draft preparation;

Daniela Boldini: Writing - Review & Editing, Validation, Supervision;

Chang Liu: Data Curation and Software;

Chuncan He: Investigation and Resources;

Shuangshuang Wu: Writing - review & editing.

Declaration of interests

☒ The authors declare that they have no known competing financial interests or personal relationships that could have appeared to influence the work reported in this paper.

☐The authors declare the following financial interests/personal relationships which may be considered as potential competing interests: